TECHNISCHE UNIVERSITÄT WIEN
Vienna | Austria

Master Thesis

Drag Reduction in a Lubricated Turbulent Channel

carried out for the purpose of obtaining the degree of Master of Science (MSc or Dipl.-Ing. or DI), submitted at TU Wien, Faculty of Mechanical and Industrial Engineering, by

Alexander Matthias Pöllinger

Mat.Nr.: 01325783
Margaretenstraße 131, 1050 Wien, Austria

under the supervision of

Univ.Prof. Dipl.-Ing. Dr.-Ing. Alfredo Soldati

Institute of Fluid Mechanics and Heat Transfer, E322

Vienna, February 2021

Author's e-mail:

alexander.m.poellinger@gmail.com

Author's address:

Institute of Fluid Mechanics and Heat Transfer
Vienna University of Technology
Tower BA/E322, Getreidemarkt 9
1060 Vienna – Austria

Cover:

Energy budgets and flow structures of a lubricated plane channel is compared to that of a single phase channel at the same power input. The viscosity ratio of the lubricant and core fluid is 0.01.

Acknowledgments

I would like to thank my supervisor Univ. Prof. Dipl.-Ing. Dr.-Ing. Alfredo Soldati without whom this work would have not been possible. I would also like to thank my co-supervisors Dr. Francesco Zonta and Dr. Alessio Roccon for their care and excellent guidance dedicating time from the first to the last day and for their constant input and support.

Best thanks to everyone involved in the procedure of the promotional grant for a scientific thesis at TU Wien, as well as the Vienna Scientific Cluster (Vienna, Austria) and CINECA supercomputing center (Bologna, Italy), for the generous allowance of computing resources.

Abstract

Direct numerical simulation (DNS) was utilized to study the drag reduction in a lubricated channel, characterized by the injection of a lubricating fluid layer in the near wall region of a planar channel to favor the transportation of the core fluid. In the present work the fluids have equal density but different viscosity, allowing for the definition of a viscosity ratio $\lambda = \eta_1/\eta_2$. In the scope of this work both a lubricated channel with $\lambda = 0.01$ and a single phase reference case were considered to quantify the drag reduction enabled by the lubricating layer and observe flow dynamics at large viscosity ratios. All DNS were run with a constant power input (CPI) approach. This allows for the power injected into the flow to be constant across both cases considered by adjusting the pressure gradient according to the flow rate of the channel. This was accomplished here by extending the CPI approach to lubricated channel flow. The dynamics of the liquid-liquid interface is described by a phase-field method (PFM).
The simulation results indicate a significant drag reduction for the lubricated case. The flow rate increase has been quantified to be $\simeq 63\,\%$. An analysis of the mean and turbulent kinetic energy budgets gives insight into the drag reduction mechanisms of the lubricated channel. For the multi-phase case, turbulence is sustained in the lubricating layer due to the local increase in Reynolds number. The core flow experiences a laminarization due to the hindering of transfer of turbulent kinetic energy from the boundary layer to the core.

Zusammenfassung

Um die Verringerung des Strömungswiderstands in einem geschmierten Rechteckskanal zu ermitteln wurde Direkte Numerischer Simulation (DNS) eingesetzt. Die vorliegende Strömung ist durch das Einbringen eines dünnen Flüssigkeitsfilms in der wandnahen Region an Ober- und Unterseite eines Rechteckskanals charakterisiert. In der vorliegenden Arbeit besitzen beide Fluide jeweils die gleiche Dichte, aber unterschiedliche Viskositäten. Dadurch lässt sich ein Viskositätsverhältnis definieren ($\lambda = \eta_1/\eta_2$). Damit wurde im Zuge dieser Arbeit eine Untersuchung am geschmierten Kanal mit $\lambda = 0.01$ durchgeführt, um die Dynamik der Strömung zu untersuchen. Weiters erlaubt eine zusätzliche einphasige Referenzsimulation eine Quantifizierung der möglichen Verringerung des Strömungswiderstands. Alle DNS wurden mittels "Constant Power Input" (CPI) Ansatz durchgeführt. Hier wird der Druckgradient als Steuergröße eingesetzt, um den Massenstrom im Kanal einzustellen. Damit ist sichergestellt, dass die dem Fluid zugeführte Leistung für beide in dieser Arbeit untersuchten Fälle gleich groß ist. Dazu musste der CPI Ansatz an mehrphasige Strömungen angepasst werden. Die Interaktionen zwischen den Fluidschichten wurden mittels "Phase-Field" Methode (PFM) modelliert.

Die Simulationsergebnisse weisen auf eine signifikante Verringerung des Strömungswiderstands hin. Dabei konnte eine Erhöhung des Massenstroms durch den Kanal von $\simeq 63\,\%$ beobachtet werden. Eine zusätzliche Analyse der mittleren und turbulent kinetischen Energie gibt weiteren Aufschluss über die Mechanismen der Widerstandsverminderung. Im Falle des mehrphasigen Kanals, wird im Schmierfilm aufgrund der lokal höheren Reynolds Zahl, turbulente Strömung beobachtet. Die viskose Kernschicht hingegen erfährt eine Laminarisierung der Strömung. Dies wird auf das Vorhandensein der Grenzschicht zwischen den Fluiden und den dadurch behinderten Transport von turbulent kinetischer Energie zurückgeführt.

Contents

1

Introduction

The friction losses in a rectangular channel are defined by the losses at the wall, as well as the viscous effects in the fluid itself. Especially in high viscosity fluids such as crude oil, it is very challenging to achieve high flow rates due to the cubic increase in pumping power requirements. Hence the demand for techniques to improve the viability of transporting high viscosity oils will increase as the extraction of heavy crude oils is becoming more common.

One idea is to lubricate the flow with water, as it is immiscible with oil, not hazardous and accessible. Due to it's low viscosity, water migrates to regions of high shear, thus creating a thin, stable lubricating layer at the wall [24]. This has been of interest in an industrial setting as patents from the first half of the 20th century show [15, 22].

The drag reduction mechanisms were later described in multiple scientific works [6, 8, 14, 23, 25], with a comprehensive overview given in [12, 24].

Literature suggests the drag reduction is mainly attributed to the viscosity difference and goes into detail on what kind of flow configurations can be observed, but few attempts have been made to quantify the drag reduction potential. Therefore the main objective of this work is to get a better understanding for the flow dynamics in the viscosity stratified lubricated channel as well as finding quantification for the drag reduction achievable utilizing this method.

This will be investigated by considering the following simplified but still relevant simulation setup: A plane channel with low-viscosity layers at both top and bottom walls with a core layer of higher-viscosity fluid. The height of a lubricating layer is defined as 7.5% of the entire channel height. Additionally a reference simulation of the same channel geometry without the lubricating layers and the same viscosity of the original core layer was considered for comparison. Method of choice was a finely-resolved

pseudo-spectral Direct Numerical Simulation (DNS) of the flow field coupled with a Phase Field Method (PFM) used to describe the interactions between the fluid layers and track the motion of the liquid-liquid interfaces.

The same numerical approach as in Ahmadi et al. [2] has been chosen, albeit the use of the Constant Power Input approach to calculate the input power into the system. In this work a power Reynolds number of $Re_{\Pi} = 81050$ was chosen for both the lubricated case as well as for the reference channel. This ensures equal power input for both cases and flow parameters can be compared conveniently. This Reynolds number is also sufficiently high to guarantee fully developed turbulent channel flow for the single phase reference case. Roccon et al. has shown a significant drag reduction for a channel with a single lubricant layer can be achieved ($\approx 24\,\%$), if turbulence is recovered within the layer [37]. The main mechanism being the lower viscosity of the lubricating layer which reduces the wall shear stresses.

The present work shows that by choosing the flow parameters correctly, one can achieve a laminarization of the core layer. Furthermore better insight on the turbulent kinetic and mean kinetic energy fluxes through the liquid-liquid interface is gained utilizing the energy box method.

2

Methodology

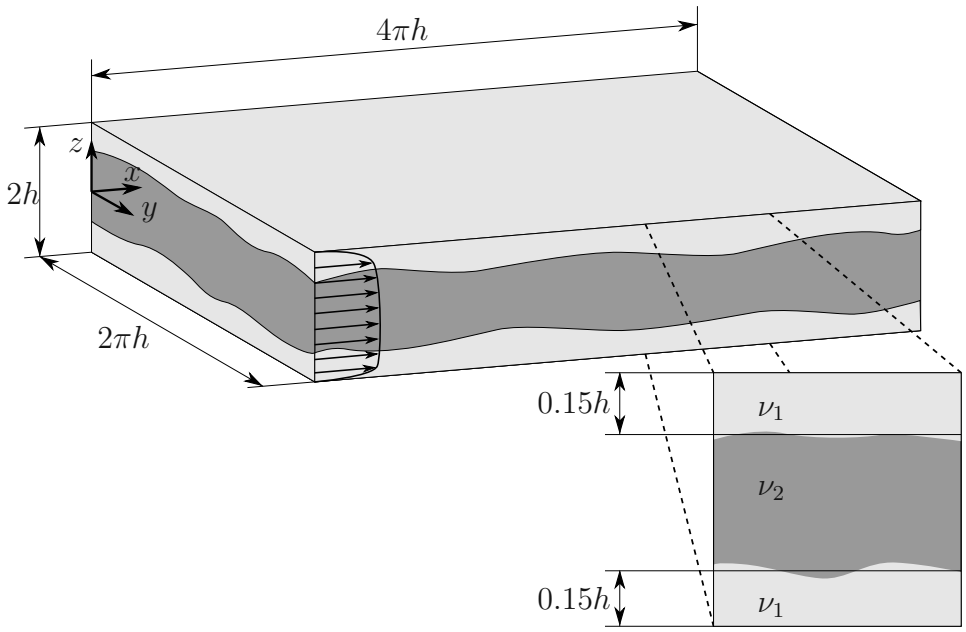

Figure 2.1 – Dimensions of the computational domain used for all simulations in this work. (For the benchmark simulation of a single-phase flow the layer height h_1 does not apply.) The z-range is symmetric around the channel center, ranging from $-h$ to h. The black lines on the zoomed in section illustrate the averaged interface position at $z = h - h_1$ while the gray shade visualizes an instantaneous position of the deformed interface at an arbitrary time t.

In the extent of the present paper the case of two immiscible fluids flowing inside a rectangular flat channel is considered. Shown in Figure 2.1, the upper and lower part of the channel is occupied by a thin lubricating layer (layers 1 and 3), each of thickness $h(1 - m)$, density ρ_1 and viscosity η_1. The core of the channel is occupied by the main fluid layer (layer 2), of thickness $2mh$, density ρ_2 and viscosity η_2. The channel has dimensions $L_x \times L_y \times L_z = 4\pi h \times 2\pi h \times 2h$ along the streamwise (x), spanwise (y) and wall-normal direction (z). This work assumes that the two fluids have equal

density ($\rho_1 = \rho_2 = \rho$) but different viscosities so that a viscosity ratio $\lambda = \eta_1/\eta_2$ can be defined. The interfaces that separates the two phases, located at distance $\pm mh$ from the channel center, is characterized by a constant value of the interfacial tension (σ). The phase-field method, used to capture the dynamics of the interface, is coupled with direct numerical simulation of the Navier-Stokes equations to describe the dynamics of the liquid-liquid flow system [5, 17, 36, 41]. The main ingredients of the proposed approach are summarized in the following section.

2.1 Phase Field Method

In the framework of the Phase Field Method (PFM), the sharp interface between the two fluids is represented by a thin transition region where the interfacial forces are applied. The basic idea of the PFM is to introduce an order parameter (or phase-field, ϕ) that varies continuously over the interfacial layers and is uniform in the bulk phases (i.e. $\phi = -1$ in the main layer and $\phi = +1$ in the thin lubricating layers). The transport of the order parameter is described by a Cahn-Hilliard equation, which in a dimensionless form reads as:

$$\frac{\partial \phi}{\partial t} + u_i \frac{\partial \phi}{\partial x_i} = \frac{1}{Pe_\Pi} \frac{\partial^2 \mu}{\partial x_i^2}, \tag{2.1}$$

where u_i is the i-th component of the velocity vector, Pe_Π is the Péclet number, and μ is the chemical potential. The Péclet number is defined as follows:

$$Pe_\Pi = \frac{u_\Pi h}{\mathcal{M}\beta}, \tag{2.2}$$

with u_Π the characteristic velocity (see Section 2.2 for details on its definition), h the channel half height, $\mathcal{M}$ the mobility and β a positive constant used to make the chemical potential dimensionless. The Péclet number represents the ratio between the diffusive time-scale, $h^2/\mathcal{M}\beta$, and the convective time-scale, h/u_Π. The chemical potential μ is defined as the functional derivative of a Ginzburg Landau free energy functional, $\mathcal{F}[\phi, \partial\phi/\partial x_i]$. The expression of the free energy functional is chosen here to represent an immiscible binary mixture of isothermal fluids [41, 42]. This functional is composed by the sum of two different contribution: the first contribution, f_0, accounts for the tendency of the system to separate into the two pure stable phases while the second

contribution, f_{mix}, is a non-local term (mixing energy) accounting for the energy stored at the interface (i.e. interfacial tension). The mathematical expression of the functional is the following:

$$\mathcal{F}[\phi, \partial\phi/\partial x_i] = \int_\Omega \Bigg(\underbrace{\frac{(\phi^2-1)^2}{4}}_{f_0} + \underbrace{\frac{Ch^2}{2}\left|\frac{\partial\phi}{\partial x_i}\right|^2}_{f_{mix}} \Bigg) d\Omega \,, \tag{2.3}$$

where Ω is the domain considered and Ch is the Cahn number. The Cahn number represents the dimensionless thickness of the interface and it is defined as follows:

$$Ch = \frac{\xi}{h} \,, \tag{2.4}$$

being ξ the dimensional value of the interface thickness and h the channel half height. From Equation (2.3), the expression of the chemical potential can be obtained by taking the variational derivative of the functional with respect to the order parameter and results in:

$$\mu = \frac{\delta\mathcal{F}[\phi, \partial\phi/\partial x_i]}{\delta\phi} = \phi^3 - \phi - Ch^2\frac{\partial^2\mu}{\partial x_i^2} \,. \tag{2.5}$$

2.2 Governing Equations

The description of the hydrodynamics is achieved by coupling the Navier-Stokes equation with a phase-field transport equation. An additional interfacial term in the Navier-Stokes equations represents the existence of interfaces and resulting forces. In this work, two phases with the same densities ($\rho = \rho_1 = \rho_2$) but different viscosities ($\eta_1 \neq \eta_2$) are considered. Under these assumptions, the continuity and Navier-Stokes equations result in:

$$\frac{\partial u_i}{\partial x_i} = 0 \,, \tag{2.6}$$

$$\begin{aligned}\frac{\partial u_i}{\partial t} + u_j\frac{\partial u_i}{\partial x_j} = -p_x\delta_{xi} - \frac{\partial p}{\partial x_i} + \frac{1}{Re_\Pi}\frac{\partial}{\partial x_j}\left[\eta(\phi)\left(\frac{\partial u_i}{\partial x_j} + \frac{\partial u_j}{\partial x_i}\right)\right] \\ + \frac{3}{\sqrt{8}}\frac{Ch}{We_\Pi}\frac{\partial\tau_{ij}^c}{\partial x_j} \,,\end{aligned} \tag{2.7}$$

where u_i is the i-th component of the velocity vector, p_x the mean stream-wise pressure gradient driving the flow [32, 40], p the pressure field, $\eta(\phi)$ the viscosity map accounting for the viscosity contrast between the two phases [1, 2], δ_{ij} the Kronecker delta and τ_{ij}^c the Korteweg tensor. The Korteweg tensor, used to account for the surface tension forces, is defined as follows:

$$\tau_{ij}^c = \left|\frac{\partial \phi}{\partial x_i}\right|^2 \delta_{ij} - \frac{\partial \phi}{\partial x_i}\frac{\partial \phi}{\partial x_j}\,. \tag{2.8}$$

In contrast to previous work [1, 2, 37] in which the flow is driven through the channel by a mean constant pressure gradient [32, 40]; in the present work a constant power input framework (CPI) is employed [11, 13], hence driving the the flow by imposing a constant pumping power, Π_m. Therefore, to keep the pumping power constant over time, the mean pressure gradient is dynamically adjusted in accordance with the overall channel flow-rate, Q_t (see appendix 2.6 for details). Employing a CPI approach, instead of the friction velocity u_τ (commonly used as reference velocity when a constant pressure gradient or a constant flow-rate approach are employed), it is more convenient to use the following characteristic velocity (Derivation can be found in appendix 2.5):

$$u_\Pi = \sqrt{\frac{\Pi_m h}{3\eta_1}}\,, \tag{2.9}$$

being η_1 the viscosity of the lubricating layer. From a physical point of view, the characteristic velocity u_Π represents the bulk velocity (i.e. the average velocity across the channel section) of a laminar flow driven by the same pumping power. The dimensionless groups appearing in Equation (2.7) are the power Reynolds number, Re_Π, and the Weber number, We_Π, which are defined as follows:

$$Re_\Pi = \frac{\rho u_\Pi h}{\eta_1}\,, \qquad We_\Pi = \frac{\rho u_\Pi^2 h}{\sigma}\,. \tag{2.10}$$

The power Reynolds number represents the ratio between the inertial and the viscous forces and it is defined using the viscosity of the main layer as a reference. The Weber number is the ratio between the inertial and the surface tension forces.

2.3 Numerical Method

The governing Equations (2.1 , 2.7 , 2.6) are solved utilizing a pseudo-spectral method, which will be described in detail in the course of the following sections.

2.3.1 Solution Algorithm

The first step is to rewrite the dimensionless governing Equations (2.1 , 2.7) and (2.6) in a formulation suitable to the solution algorithm. This is achieved by rewriting the Navier-Stokes and continuity equations in the "wall-normal-velocity normal-vorticity" formulation. The Cahn-Hilliard equation is rewritten adopting a particular "operator-splitting" technique. A schematic representation of the solution procedure is shown in Figure 2.2.

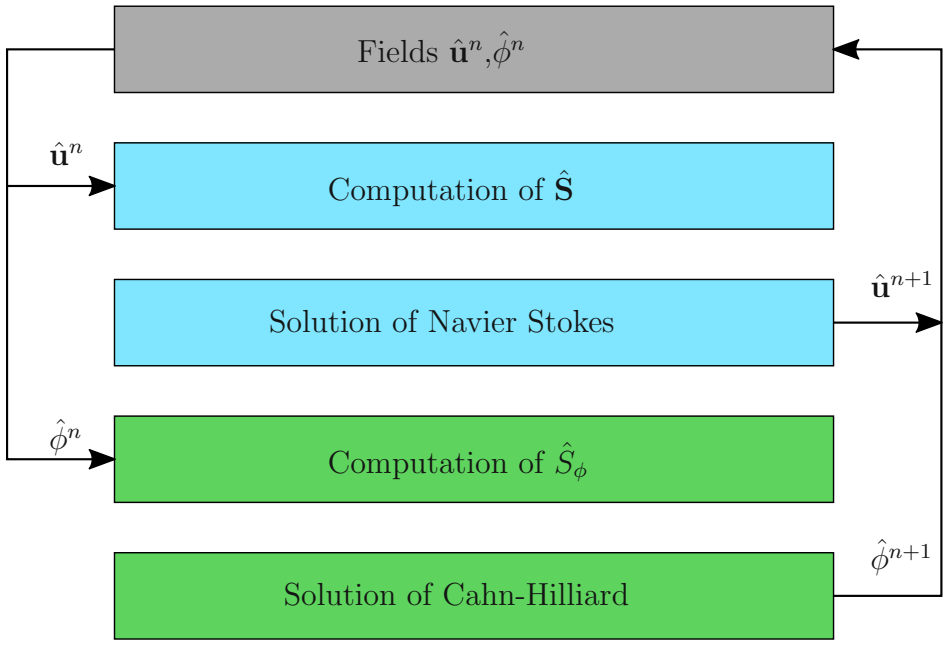

Figure 2.2 – Scheme of the numerical solver used. From the initial fields $\hat{\mathbf{u}}^n$, $\hat{\phi}^n$ at the step n, for each equation the non linear terms are computed in physical space then transformed back into spectral space. After this operation the unknown field variables at time $n+1$ can be computed utilizing the Helmholtz solver.

Velocity-Vorticity Formulation

Bringing the momentum Equation (2.7) into a dimensionless form, it can be rewritten in the following way (superscripts removed for legibility):

$$\frac{\partial \mathbf{u}}{\partial t} = -\nabla p' + \mathbf{S} + \frac{1}{Re_\Pi}\nabla^2 \mathbf{u}, \tag{2.11}$$

where the pressure term p has been decomposed in fluctuating and mean components, $p = p' + \overline{p}$. The mean pressure gradient $\Pi = \nabla \overline{p}$ as well as all non-linear terms have been collected into the term $\mathbf{S}$:

$$\begin{aligned} \mathbf{S} = \; & - \; \mathbf{u} \cdot \nabla \mathbf{u} + p_x + \frac{1}{Re_\Pi}\nabla \cdot (\eta(\phi)(\nabla \mathbf{u} + \nabla \mathbf{u}^T)) \\ & + \; \frac{3}{\sqrt{8}}\frac{Ch}{We_\Pi}\nabla \cdot (|\nabla \phi|^2 \mathbf{I} - \nabla \phi \otimes \nabla \phi) \end{aligned} \tag{2.12}$$

To solve the system composed by the Equation (2.6) and Equation (2.7), the fluctuating pressure term $\nabla p'$ is removed by taking the curl of Equation (2.11), as result the transport equation for the vorticity $\boldsymbol{\omega}$ is obtained:

$$\frac{\partial \boldsymbol{\omega}}{\partial t} = \nabla \times \mathbf{S} + \frac{1}{Re_\Pi}\nabla^2 \boldsymbol{\omega} \tag{2.13}$$

where the identity $\nabla \times \nabla p' = 0$ has been used. Taking twice the curl of Equation (2.11), substituting Equation (2.6) and the identity $\nabla \times \nabla \times \mathbf{c} = \nabla(\nabla \cdot \mathbf{c}) - \nabla^2 \mathbf{c}$, the following 4^{th}-order equation for the velocity $\mathbf{u}$ is obtained:

$$\frac{\partial \nabla^2 \mathbf{u}}{\partial t} = \nabla^2 \mathbf{S} - \nabla(\nabla \cdot \mathbf{S}) + \frac{1}{Re_\Pi}\nabla^4 \mathbf{u} \tag{2.14}$$

Equations (2.13 - 2.14) are solved for the wall-normal components of the vorticity ω_z and velocity w, adopting the "velocity - vorticity" algorithm developed by [27]; rewriting Equations (2.13 - 2.14) for ω_z and w, respectively, the following equations are obtained:

$$\frac{\partial \omega_z}{\partial t} = \frac{\partial S_y}{\partial x} - \frac{\partial S_x}{\partial y} + \frac{1}{Re_\Pi}\nabla^2 \omega_z \tag{2.15}$$

$$\frac{\partial (\nabla^2 w)}{\partial t} = \nabla^2 S_z - \frac{\partial}{\partial z}\left(\frac{\partial S_x}{\partial x} + \frac{\partial S_y}{\partial y} + \frac{\partial S_z}{\partial z}\right) + \frac{1}{Re_\Pi}\nabla^4 w \tag{2.16}$$

With a suitable set of boundary conditions, ω_z and w are computed and then the streamwise u and the spanwise v velocity components are obtained from the continuity equation and the definition of vorticity:

$$\frac{\partial w}{\partial z} = -\frac{\partial u}{\partial x} - \frac{\partial v}{\partial y} \tag{2.17}$$

$$\omega_z = \frac{\partial v}{\partial x} - \frac{\partial u}{\partial y} \tag{2.18}$$

Once the velocity field is obtained, the fluctuating pressure p' can be obtained by solving a Poisson-type equation:

$$\nabla^2 p' = \nabla \cdot \mathbf{S} \tag{2.19}$$

Cahn-Hilliard Equation Splitting

The solution of the Cahn-Hilliard equation requires robust numerical schemes due to the high order operators that it involves; expanding Equation (2.1), a 4^{th}-order operator is highlighted:

$$\frac{\partial \phi}{\partial t} = -\mathbf{u} \cdot \nabla \phi + \frac{1}{Pe_\phi}\left(\nabla^2 \phi^3 - \nabla^2 \phi - Ch^2 \nabla^4 \phi\right) \tag{2.20}$$

To reduce the stability requirements and adopt the same pseudo-spectral scheme involved for the momentum equation, Equation (2.20) is rewritten in the following way:

$$\frac{\partial \phi}{\partial t} = S_\phi + \frac{s Ch^2}{Pe_\phi}\nabla^2 \phi - \frac{Ch^2}{Pe_\phi}\nabla^4 \phi \tag{2.21}$$

The operator splitting $\nabla^2 \phi = \nabla^2 \phi (s Ch^2 + 1) - s Ch^2 \nabla^2 \phi$ is similar to the one adopted by [45] and is obtained through a positive coefficient s that is chosen considering the temporal discretization; similar procedures can be found in [5, 29]. The convective term, the non-linear term and the terms rising from the operator splitting are collected in the term S_ϕ:

$$S_\phi = -\mathbf{u} \cdot \nabla \phi + \frac{1}{Pe_\phi}\nabla^2 \phi^3 - \frac{(s Ch^2 + 1)}{Pe_\phi}\nabla^2 \phi \tag{2.22}$$

2.3.2 Spectral Approximation

The Equations (2.15 - 2.16) and (2.20) are solved adopting a pseudo-spectral spatial discretization: solutions are approximated by Fourier transforms along the two periodic directions of the channel geometry x and y, respectively; Chebyshev polynomials are adopted to approximate the solution along the wall-normal direction. In order to avoid convolutions in the Fourier-Chebyshev space, the multiplication of spectral variables (i.e. convective terms) is obtained transforming back the variables to the physical space, taking the multiplications and the re-transforming to the Fourier-Chebyshev space. For this reason these class of algorithms is also known as "pseudo-spectral algorithms". A signal g, projected in to the Fourier space along the periodic directions x and y, can be represented by the following sum of harmonics:

$$g(x,y,z) = \sum_{n_x=-\frac{N_x}{2}+1}^{\frac{1}{2}N_x} \sum_{n_y=-\frac{N_y}{2}+1}^{\frac{1}{2}N_y} \hat{g}(k_x,k_y,z) e^{j(k_x x + k_y y)} \tag{2.23}$$

where $j = \sqrt{-1}$ is the imaginary unit of the complex representation, $\hat{g}$ is the Fourier coefficient of the signal in the modal coordinates (k_x, k_y); at this point dependence on the physical coordinate z is still present. The two periodic directions are treated with a Fast Fourier Transform (FFT) algorithm imposing periodicity lengths of L_x and L_y and projecting the velocity vector on to N_x and N_y Fourier modes in the x and y directions of the geometry of Figure 2.1. Through the Fourier transform, the variables are mapped an a uniform grid in the physical space. The nodes spacing is defined as:

$$\Delta x = \frac{L_x}{N_x - 1} \qquad \Delta y = \frac{L_y}{N_y - 1} \tag{2.24}$$

The signal is decomposed in a sum of periodical functions characterized by wavenumber and amplitude; the former represents the frequency of the corresponding harmonic, whereas the latter is the magnitude of the harmonic. Each mode n_x or n_y is characterized by the following wave-numbers:

$$k_x = \frac{2\pi n_x}{L_x}, \qquad k_y = \frac{2\pi n_y}{L_y} \tag{2.25}$$

Since the Fourier basis is orthogonal, the Fourier transform $\hat{g}$ can be obtained as follows:

$$\hat{g}(k_x, k_y, z) = \frac{1}{N_x N_y} \sum_{n_x=-\frac{N_x}{2}+1}^{\frac{N_x}{2}} \sum_{n_y=-\frac{N_y}{2}+1}^{\frac{N_y}{2}} g(x, y, z) e^{-j(k_x x + k_y y)} \tag{2.26}$$

Along the wall normal direction z, the transformed signal $\hat{g}(k_x, k_y, z)$ is approximated through the sum of Chebyshev polynomials $T_n(z)$:

$$\hat{g}(k_x, k_y, z) = \sum_{n_z=0}^{N_z'} h(k_x, k_y, n_z) T_n(z) \tag{2.27}$$

where the prime indicate the first term halving. The Chebyshev polynomial of order n_z in z is defined as follows:

$$T_{nz}(z) = \cos\left[n_z \arccos(z)\right] \tag{2.28}$$

where n_z is one of the N_z Chebyshev modes and $-1 \leq z \leq 1$. The orthogonality property holds also for the Chebyshev polynomials and the inverse transform is:

$$\hat{h}(k_x, k_y, n_z) = \frac{2}{N_z} \sum_{n_z=0}^{N_z'} \hat{g}(k_x, k_y, z) T_n(z) \tag{2.29}$$

The variables described in the Chebyshev space are mapped in the physical space according to the following mapping:

$$z = \cos\left(\frac{n_z \pi}{N_z}\right) \tag{2.30}$$

With adoption of Chebyshev polynomials for the approximation of the solution along the wall-normal direction, the spatial discretization is characterized by a large resolution near the walls ($z = \pm 1$), where large velocity gradients need to be resolved. A complete review of the method can be found in [7]. Concluding, adopting the transformations of Equations (2.23 - 2.27), the spectral representation of a three-dimensional signal is the

following:

$$g(x,y,z,t) = \sum_{n_x=-\frac{N_x}{2}+1}^{\frac{1}{2}N_x} \sum_{n_y=-\frac{N_y}{2}+1}^{\frac{1}{2}N_y} \sum_{n_z=0}^{N_z'} \hat{h}(k_x,k_y,n_z,t) T_{n,z}(z) e^{j(k_x x + k_y y)} \tag{2.31}$$

Due to the presence of products taken in to the physical space, the computational algorithm needs the introduction of de-aliasing procedures also in the Chebyshev transforms; following [7] the "2/3 rule" is applied, keeping only the first two thirds of the modes after the application of the pseudo-spectral multiplications.

2.3.3 Discretization and Solution of the Equations

Velocity Equation

Using the spectral representation of Section 2.3.2, Equation (2.16) reads:

$$\begin{aligned} \frac{\partial}{\partial t}\left(\frac{\partial^2}{\partial z^2} - k_{xy}^2\right)\hat{w} &= \left(\frac{\partial^2}{\partial z^2} - k_{xy}^2\right)\hat{S}_z \\ &- \frac{\partial}{\partial z}\left(ik_x\hat{S}_x + ik_y\hat{S}_y + \frac{\partial}{\partial z}\hat{S}_z\right) \\ &+ \frac{1}{Re_\Pi}\left(\frac{\partial^2}{\partial z^2} - k_{xy}^2\right)\left(\frac{\partial^2}{\partial z^2} - k_{xy}^2\right)\hat{w} \end{aligned} \tag{2.32}$$

where $k_{xy}^2 = k_x^2 + k_y^2$. The equation above stresses that the z derivatives are taken in a different way, due to the adoption of Chebyshev polynomials. Equation (2.32) is discretized in time adopting an hybrid IMplicit EXplicit (IMEX) scheme: (i) a second-order Adams-Bashfort explicit scheme is adopted for the non-linear convective terms; (ii) the implicit Crank-Nicholson implicit scheme is applied to the diffusive

operators. The time-discretized form of Equation (2.32) reads:

$$\begin{aligned}
&\frac{1}{\Delta t}\left[\left(\frac{\partial^2}{\partial z^2}-k_{xy}^2\right)\hat{w}^{n+1}-\left(\frac{\partial^2}{\partial z^2}-k_{xy}^2\right)\hat{w}^{n}\right]= \\
&\frac{3}{2}\left(\frac{\partial^2}{\partial z^2}-k_{xy}^2\right)\hat{S}_z^n-\frac{1}{2}\left(\frac{\partial^2}{\partial z^2}-k_{xy}^2\right)\hat{S}_z^{n-1} \\
-\;&\frac{3}{2}\frac{\partial}{\partial z}\left(ik_x\hat{S}_x^n+ik_y\hat{S}_y^n+\frac{\partial}{\partial z}\hat{S}_z^n\right) \\
+\;&\frac{1}{2}\frac{\partial}{\partial z}\left(ik_x\hat{S}_x^{n-1}+ik_y\hat{S}_y^{n-1}+\frac{\partial}{\partial z}\hat{S}_z^{n-1}\right) \\
+\;&\frac{1}{Re_\Pi}\left(\frac{\partial^2}{\partial z^2}-k_{xy}^2\right)\left(\frac{\partial^2}{\partial z^2}-k_{xy}^2\right)\frac{\hat{w}^{n+1}-\hat{w}^n}{2}
\end{aligned} \tag{2.33}$$

where superscripts $n-1$, n, $n+1$ indicate the three consecutive time levels $t-\Delta t$, t and $t+\Delta t$, respectively and Δt is the time-step. Equation (2.33) is rearranged and, introducing the coefficient $\gamma = \Delta t/2Re_\Pi$, the following is obtained:

$$\begin{aligned}
&\left[1-\gamma\left(\frac{\partial^2}{\partial z^2}-k_{xy}^2\right)\right]\left(\frac{\partial^2}{\partial z^2}-k_{xy}^2\right)\hat{w}^{n+1}= \\
+\;&\frac{3\Delta t}{2}\left(\frac{\partial^2}{\partial z^2}-k_{xy}^2\right)\hat{S}_z^n-\frac{\Delta t}{2}\left(\frac{\partial^2}{\partial z^2}-k_{xy}^2\right)\hat{S}_z^{n-1} \\
-\;&\frac{3\Delta t}{2}\frac{\partial}{\partial z}\left(ik_x\hat{S}_x^n+ik_y\hat{S}_y^n+\frac{\partial}{\partial z}\hat{S}_z^n\right) \\
+\;&\frac{\Delta t}{2}\frac{\partial}{\partial z}\left(ik_x\hat{S}_x^{n-1}+ik_y\hat{S}_y^{n-1}+\frac{\partial}{\partial z}\hat{S}_z^{n-1}\right) \\
+\;&\left[\gamma\frac{\partial^2}{\partial z^2}+(1-k_{xy}^2)\right]\left(\frac{\partial^2}{\partial z^2}-k_{xy}^2\right)\hat{w}^n
\end{aligned} \tag{2.34}$$

The discretized form ot the continuity equation is:

$$ik_x\hat{u}+ik_y\hat{v}+\frac{\partial w}{\partial z}=0 \tag{2.35}$$

Substituting Equation (2.35) into Equation. (2.34) and introducing the coefficient $\lambda^2 = (1 + \gamma k_{xy}^2)/\gamma$, the following is obtained:

$$\begin{aligned} - \quad & \gamma \left(\frac{\partial^2}{\partial z^2} - \lambda^2 \right) \left(\frac{\partial^2}{\partial z^2} - k_{xy}^2 \right) \hat{w}^{n+1} = \\ - \quad & k_{xy}^2 \left(\frac{3}{2} \hat{S}_z^n - \frac{1}{2} \hat{S}_z^{n-1} \right) \Delta t - k_{xy}^2 \left[\gamma \frac{\partial^2}{\partial z^2} + \left(1 - \gamma k_{xy}^2 \right) \right] \hat{w}^n \\ - \quad & \frac{\partial}{\partial z} i k_x \left(\frac{3}{2} \hat{S}_x^n - \frac{1}{2} \hat{S}_x^{n-1} \right) \Delta t - \frac{\partial}{\partial z} i k_x \left(\gamma \frac{\partial^2}{\partial z^2} + \left(1 - \gamma k_{xy}^2 \right) \right) \hat{u}^n \\ - \quad & \frac{\partial}{\partial z} i k_y \left(\frac{3}{2} \hat{S}_y^n - \frac{1}{2} \hat{S}_y^{n-1} \right) \Delta t - \frac{\partial}{\partial z} i k_y \left(\gamma \frac{\partial^2}{\partial z^2} + \left(1 - \gamma k_{xy}^2 \right) \right) \hat{v}^n \end{aligned} \tag{2.36}$$

The historical terms $\hat{H}_x^n$, $\hat{H}_y^n$ and $\hat{H}_z^n$ are defined as follows:

$$\begin{aligned} \hat{H}_x^n &= \left(\frac{3}{2} \hat{S}_x^n - \frac{1}{2} \hat{S}_x^{n-1} \right) \Delta t + \left[\gamma \frac{\partial^2}{\partial z^2} + \left(1 - \gamma k_{xy}^2 \right) \right] \hat{u}^n \\ \hat{H}_y^n &= \left(\frac{3}{2} \hat{S}_y^n - \frac{1}{2} \hat{S}_y^{n-1} \right) \Delta t + \left[\gamma \frac{\partial^2}{\partial z^2} + \left(1 - \gamma k_{xy}^2 \right) \right] \hat{v}^n \\ \hat{H}_z^n &= \left(\frac{3}{2} \hat{S}_z^n - \frac{1}{2} \hat{S}_z^{n-1} \right) \Delta t + \left[\gamma \frac{\partial^2}{\partial z^2} + \left(1 - \gamma k_{xy}^2 \right) \right] \hat{w}^n \end{aligned} \tag{2.37}$$

introducing Equation (2.37), Equation (2.36) reads:

$$\left(\frac{\partial^2}{\partial z^2} - \lambda^2 \right) \left(\frac{\partial^2}{\partial z^2} - k_{xy}^2 \right) \hat{w}^{n+1} = \frac{1}{\gamma} \left[k_{xy}^2 \hat{H}_z^n + \frac{\partial}{\partial z} \left(i k_x \hat{H}_x^n + i k_y \hat{H}_y^n \right) \right] \tag{2.38}$$

Collecting $\hat{H}^n = k_{xy}^2 \hat{H}_z^n + \frac{\partial}{\partial z}(i k_x \hat{H}_x^n + i k_y \hat{H}_y^n)$ the final form of the discretized Equation (2.16) is obtained:

$$\left(\frac{\partial^2}{\partial z^2} - \lambda^2 \right) \left(\frac{\partial^2}{\partial z^2} - k_{xy}^2 \right) \hat{w}^{n+1} = \frac{\hat{H}^n}{\gamma} \tag{2.39}$$

We can introduce the auxiliary variable $\hat{\theta} = \left(\frac{\partial^2}{\partial z^2} - k_{xy}^2 \right) \hat{w}^{n+1}$ and the 4^{th}-order equation can be split in two 2^{nd}-order equations:

$$\left(\frac{\partial^2}{\partial z^2} - \lambda^2 \right) \hat{\theta} = \frac{\hat{H}^n}{\gamma} \tag{2.40}$$

$$\left(\frac{\partial^2}{\partial z^2} - k_{xy}^2 \right) \hat{w}^{n+1} = \hat{\theta} \tag{2.41}$$

Equation (2.40) and Equation (2.41) can be solved imposing different boundary conditions, for a closed channel (no-slip at both the walls) the following BC are applied.

$$\hat{w}^{n+1}(\pm 1) = 0 \qquad \frac{\partial \hat{w}^{n+1}}{\partial z}(\pm 1) = 0 \tag{2.42}$$

While for an open channel the following boundary conditions are applied.

$$\hat{w}^{n+1}(-1) = 0, \qquad \frac{\partial \hat{w}^{n+1}}{\partial z}(-1) = 0 \tag{2.43}$$

$$\hat{w}^{n+1}(+1) = 0, \qquad \frac{\partial^2 \hat{w}^{n+1}}{\partial z^2}(+1) = 0 \tag{2.44}$$

Both the boundary conditions are obtained from the non-slip or free-slip condition at the wall coupled with the continuity equation. The solution of Equation (2.39) requires a set of boundary conditions on $\hat{\theta}$ that lack in the physical model definition, only for the free-slip we can have a boundary condition on $\hat{\theta}$, to circumvent this problem, $\hat{\theta}$ is rewritten as follows:

$$\hat{\theta} = \hat{\theta}_1 + \hat{A}\theta_2 + \hat{B}\theta_3 \tag{2.45}$$

where $\hat{A}$ and $\hat{B}$ are complex constants to be determined. The three components, $\hat{\theta}_1$, θ_2 and θ_3 are the particular solution and two homogeneous solutions of Equation (2.40), respectively. Their solution is obtained as follows:

$$\left(\frac{\partial^2}{\partial z^2} - \lambda^2\right)\hat{\theta}_1 = \frac{\hat{H}^n}{\gamma} \qquad \hat{\theta}_1(-1) = 0 \qquad \hat{\theta}_1(+1) = 0 \tag{2.46}$$

$$\left(\frac{\partial^2}{\partial z^2} - \lambda^2\right)\theta_2 = 0 \qquad \theta_2(-1) = 1 \qquad \theta_2(+1) = 0 \tag{2.47}$$

$$\left(\frac{\partial^2}{\partial z^2} - \lambda^2\right)\theta_3 = 0 \qquad \theta_3(-1) = 0 \qquad \theta_3(+1) = 1 \tag{2.48}$$

In a similar way, also $\hat{w}^{n+1}$ is rewritten as a sum of a particular solution $\hat{w}_1$ and two homogeneous solutions w_2, w_3:

$$\hat{w}^{n+1} = \hat{w}_1 + \hat{A}w_2 + \hat{B}w_3 \tag{2.49}$$

Similarly to the solution of $\hat{\theta}$, the solutions for $\hat{w}_1$, w_2 and w_3 can be obtained applying the no-slip BC:

$$\left(\frac{\partial^2}{\partial z^2} - k_{xy}^2\right)\hat{w}_1 = \hat{\theta} \qquad \hat{w}_1(-1) = 0 \qquad \hat{w}_1(+1) = 0 \tag{2.50}$$

$$\left(\frac{\partial^2}{\partial z^2} - k_{xy}^2\right)w_2 = \theta_1 \qquad w_2(-1) = 0 \qquad w_2(+1) = 0 \tag{2.51}$$

$$\left(\frac{\partial^2}{\partial z^2} - k_{xy}^2\right)w_3 = \theta_2 \qquad w_3(-1) = 0 \qquad w_3(+1) = 0 \tag{2.52}$$

The unknown constants $\hat{A}$ and $\hat{B}$ are determined, for a closed channel, applying the $\partial\hat{w}^{n+1}/\partial z = 0$ boundary condition:

$$\frac{\partial\hat{w}_1}{\partial z}(-1) + \hat{A}\frac{\partial w_2}{\partial z}(-1) + \hat{B}\frac{\partial w_3}{\partial z}(-1) = 0 \tag{2.53}$$

$$\frac{\partial\hat{w}_1}{\partial z}(+1) + \hat{A}\frac{\partial w_2}{\partial z}(+1) + \hat{B}\frac{\partial w_3}{\partial z}(+1) = 0 \tag{2.54}$$

Or for an open channel:

$$\frac{\partial\hat{w}_1}{\partial z}(-1) + \hat{A}\frac{\partial w_2}{\partial z}(-1) + \hat{B}\frac{\partial w_3}{\partial z}(-1) = 0, \tag{2.55}$$

$$\frac{\partial^2\hat{w}_1}{\partial z^2}(+1) + \hat{A}\frac{\partial^2 w_2}{\partial z^2}(+1) + \hat{B}\frac{\partial^2 w_3}{\partial z^2}(+1) = 0 \tag{2.56}$$

Alternatively the boundary conditions at the free-slip wall (2.56) can be directly forced on the solution of $\hat{\theta}$. From Equations (2.53 - 2.56), $\hat{w}^{n+1}$ is obtained, the solutions of Equations (2.40 - 2.41) are obtained adopting the Chebysev-Tau solution algorithm proposed in [27] and the resulting tridiagonal equations system is solved adopting the Gauss elimination procedure.

Vorticity Equation

Using the spectral representation of Section 2.3.2, Equation (2.15) reads:

$$\frac{\partial\hat{\omega}_z}{\partial t} = ik_x\hat{S}_y - ik_y\hat{S}_x + \frac{1}{Re_\Pi}\left(\frac{\partial^2}{\partial z^2} - k_{xy}^2\right)\hat{\omega}_z \tag{2.57}$$

Where as before $k_{xy}^2 = k_x^2 + k_y^2$. Vorticity equation as the velocity equation is discretized in time adopting an hybrid IMplicit EXplicit (IMEX) scheme.

1. A second-order Adams-Bashfort scheme is used for the non-linear terms.

2. An implicit Crank-Nicholson is used for the diffusive term.

Using this time discretisation scheme, the equation became:

$$\begin{aligned}\frac{\hat{\omega_z}^{n+1} - \hat{\omega_z}^{n}}{\Delta t} &= \frac{3}{2}\left(ik_x\hat{S_y^n} - ik_y\hat{S_x^n}\right) \\ &- \frac{1}{2}\left(ik_x\hat{S_y^{n-1}} - ik_y\hat{S_x^{n-1}}\right) \\ &+ \frac{1}{2Re_\Pi}\left(\frac{\partial^2}{\partial z^2} - k_{xy}^2\right)\left(\hat{\omega_z}^{n+1} - \hat{\omega_z}^{n}\right)\end{aligned} \tag{2.58}$$

Where superscripts $n-1$, n, $n+1$ indicate the three consecutive time levels $t - \Delta t$, t and $t + \Delta t$, respectively. Using the definition of $\hat{\omega_z} = ik_x\hat{u_2} - ik_y\hat{u_1}$ the equation can be rewritten as:

$$\begin{aligned}\frac{\hat{\omega_z}^{n+1} - \hat{\omega_z}^{n}}{\Delta t} &= ik_x\left[\left(\frac{3}{2}\hat{S_y}^{n} - \frac{1}{2}\hat{S_y}^{n}\right)\Delta t + \frac{1}{2Re_\Pi}\left(\frac{\partial^2}{\partial z^2} - k_{xy}^2\right)\hat{v}^n\right] \\ &- ik_y\left[\left(\frac{3}{2}\hat{S_x}^{n} - \frac{1}{2}\hat{S_x}^{n}\right)\Delta t + \frac{1}{2Re_\Pi}\left(\frac{\partial^2}{\partial z^2} - k_{xy}^2\right)\hat{u}^n\right] \\ &+ \frac{1}{2Re_\Pi}\left(\frac{\partial^2}{\partial z^2} - k_{xy}^2\right)\hat{\omega_z}^{n+1}\end{aligned} \tag{2.59}$$

Defining γ as before, using the previously defined historical terms $\hat{H}_y^n$ and $\hat{H}_x^n$ and collecting $\hat{\omega^{n+1}}$ on the left size we obtain:

$$\left(\frac{\partial^2}{\partial z^2} - \beta^2\right)\hat{\omega}_z^{n+1} = -\frac{1}{\gamma}\left[ik_x\hat{H}_y^n - ik_y\hat{H}_x^n\right] \tag{2.60}$$

Where β has been defined as:

$$\beta^2 = \frac{1 + \gamma k_{xy}^2}{\gamma} \tag{2.61}$$

The solution of Equation (2.60) is obtained adopting the Chebyshev-Tau algorithm with the following BC for a closed channel:

$$\hat{\omega}_z^{n+1}(\pm 1) = 0 \tag{2.62}$$

Or for an open channel:

$$\hat{\omega}_z^{n+1}(-1) = 0 \qquad \frac{\partial \hat{\omega}_z^{n+1}}{\partial z}(+1) = 0 \tag{2.63}$$

The resulting tridiagonal equations system is then solved adopting a Gauss elimination technique. Once the wall-normal vorticity component $\hat{\omega}_z$ is known, the other two velocity components $\hat{u}^{n+1}$ and $\hat{v}^{n+1}$ can be derived from the spectral representation of the vorticity definition and the spectral representation of the continuity equation:

$$-ik_y\hat{u}^{n+1} + ik_x\hat{v}^{n+1} = \hat{\omega}_z^{n+1} \tag{2.64}$$

$$-ik_x\hat{u}^{n+1} + ik_y\hat{v}^{n+1} = \frac{\partial \hat{w}^{n+1}}{\partial z} \tag{2.65}$$

Cahn-Hilliard Equation

Equation (2.22) is discretized in space adopting the spectral representation shown in Section 2.3.2 and applied in Section 2.3.3:

$$\begin{aligned} \frac{\partial \hat{\phi}}{\partial t} &= \hat{S}_\phi + s\frac{Ch^2}{Pe}\left(\frac{\partial^2}{\partial z^2} - k_{xy}^2\right)\hat{\phi} \\ &- \frac{Ch^2}{Pe}\left(\frac{\partial^2}{\partial z^2} - k_{xy}^2\right)\left(\frac{\partial^2}{\partial z^2} - k_{xy}^2\right)\hat{\phi} \end{aligned} \tag{2.66}$$

The solution of the Cahn-Hilliard is characterized by high frequency harmonics that need to be dampened in order to keep the solution bound. The adoption of weakly damping schemes, such as the Crank-Nicholson adopted for the velocity field equations leads to aliased solutions [4]. For this reason, following [45], a 1^{st}-order Backward Difference Formula (BDF) is adopted. In particular the non-linear convective S_ϕ term is discretized adopting a 2^{nd} order Adams-Bashfort:

$$\begin{aligned} \frac{\hat{\phi}^{n+1} - \hat{\phi}^n}{\Delta t} &= \frac{3}{2}\hat{S}_\phi^n - \frac{1}{2}\hat{S}_\phi^{n-1} + s\frac{Ch^2}{Pe}\left(\frac{\partial^2}{\partial z^2} - k_{xy}^2\right)\hat{\phi}^{n+1} \\ &- \frac{Ch^2}{Pe}\left(\frac{\partial^2}{\partial z^2} - k_{xy}^2\right)\left(\frac{\partial^2}{\partial z^2} - k_{xy}^2\right)\hat{\phi}^{n+1} \end{aligned} \tag{2.67}$$

Introducing the coefficient $\gamma_\phi = (\Delta t Ch^2)/Pe$, Equation (2.67) yields:

$$\left[\frac{1}{\gamma_\phi} - s\left(\frac{\partial^2}{\partial z^2} - k_{xy}^2\right) + \left(\frac{\partial^2}{\partial z^2} - k_{xy}^2\right)^2\right]\hat{\phi}^{n+1} = \frac{\hat{H}_\phi}{\gamma_\phi} \tag{2.68}$$

where the historical term $\hat{H}_\phi$ has been introduced:

$$\frac{\hat{H}_\phi}{\gamma_\phi} = \frac{1}{\gamma_\phi}\left(\hat{\phi}^n + \frac{3\Delta t}{2}\hat{S}_\phi^n - \frac{\Delta t}{2}\hat{S}_\phi^{n-1}\right) \tag{2.69}$$

We can decompose Equation (2.68), a 4^{th} order equation, in two equivalent second order equations.

$$\begin{gathered}\left[\frac{1}{\gamma_\phi} - s\left(\frac{\partial^2}{\partial z^2} - k_{xy}^2\right) + \left(\frac{\partial^2}{\partial z^2} - k_{xy}^2\right)^2\right] = \\ \left[\left(\frac{\partial^2}{\partial z^2} - k_{xy}^2 - \lambda_1\right)\left(\frac{\partial^2}{\partial z^2} - k_{xy}^2 - \lambda_2\right)\right]\end{gathered} \tag{2.70}$$

The values of λ_1 and λ_2 can be obtained from the equation:

$$\gamma_\phi\lambda^2 - s\gamma_\phi\lambda + 1 = 0 \tag{2.71}$$

Obtaining:

$$\lambda_{1/2} = -\frac{s}{2} \pm \frac{\sqrt{s^2\gamma_\phi^2 - 4\gamma_\phi}}{2\gamma_\phi} \tag{2.72}$$

The root square poses some constraints on the choice of the value of s, in particular for having two real solutions must be:

$$s \geq \sqrt{\frac{4}{\gamma}} = \sqrt{\frac{4Pe}{\Delta t Ch^2}} \tag{2.73}$$

The choice of two coincident solutions $\lambda_1 = \lambda_2 = -s/2 = \sqrt{Pe/\Delta t Ch^2}$ guarantees the achievement of the maximum stability, under this assumption the equation for ϕ is:

$$\left(\frac{\partial^2}{\partial z^2} - k_{xy}^2 + \frac{s}{2}\right)^2\hat{\phi}^{n+1} = \frac{\hat{H}_\phi}{\gamma_\phi} \tag{2.74}$$

Defining the auxiliary variable $\theta_\phi = s\phi/2 + \nabla^2\phi$, the 4^{th} order Equation (2.68) is now split in two 2^{nd} order equations:

$$\left(\frac{\partial^2}{\partial z^2} - \delta^2\right)\hat{\theta}_\phi = \frac{\hat{H}_\phi}{\gamma_\phi} \tag{2.75}$$

$$\left(\frac{\partial^2}{\partial z^2} - \delta^2\right)\hat{\phi}^{n+1} = \hat{\theta}_\phi \tag{2.76}$$

Where $\delta^2 = k_{xy}^2 - s/2$. Equations (2.75) and (2.76) are solved imposing the following boundary conditions that emerge imposing a normal contact angle for the interface at the walls and a no-flux of chemical potential through the walls.

$$\frac{\partial\hat{\phi}^{n+1}}{\partial z}(\pm 1) = 0 \qquad \frac{\partial^3\hat{\phi}^{n+1}}{\partial z^3}(\pm 1) = 0 \tag{2.77}$$

The boundary conditions on $\hat{\theta}_\phi$ are on the first and third derivative, so there is no need to apply the influence matrix method, since:

$$\frac{\partial}{\partial z}\left(\frac{\partial^2}{\partial z^2} - \delta^2\right)\hat{\phi}^{n+1} = \frac{\partial^3\hat{\phi}^{n+1}}{\partial z^3} = \frac{\partial\hat{\theta}_\phi^{n+1}}{\partial z} \tag{2.78}$$

As consequence, Equation (2.75) is solved using the following boundary conditions:

$$\frac{\partial\hat{\theta}_\phi^{n+1}}{\partial z}(\pm 1) = 0 \tag{2.79}$$

and Equation (2.76) is solved using the following boundary conditions:

$$\frac{\partial\hat{\phi}}{\partial z}(\pm 1) = 0 \tag{2.80}$$

The solutions of Equations (2.75 - 2.76) are obtained adopting the Chebyshev-Tau solution algorithm proposed in [27] and the resulting tridiagonal equations system is solved through a Gauss elimination procedure.

Code Implementation

The numerical algorithm presented in Section 2.3 for the solution of equations presented in Section 2 has been implemented in an in-house code using Fortran-2003 as program-

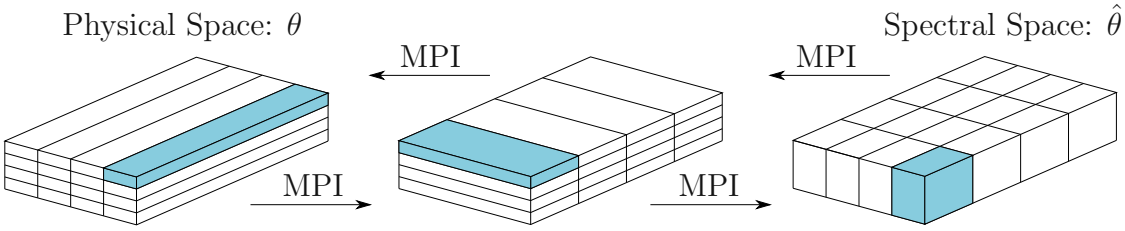

Figure 2.3 – From left to right, the unknown is in the physical space, θ, the FFT along the x direction is computed. Then, through MPI-communications, the pencil is reoriented and the FFT along the y direction is performed. Last, the pencil is again reoriented and the Chebyshev transform along the z direction is computed. After these steps, the unknown is described in the spectral space, $\hat{\theta}$. The inverse transform can be computed following the same steps but in the opposite direction.

ming language. The code is parallelized using an MPI paradigm and adopting a 2D domain decomposition. Considering a generic variable θ, in the physical space, each rank has a pencil with dimensions $N_x \times N_{yp} \times N_{zp}$, where N_{yp} and N_{zp} are a fraction of the total number of nodes used along the y and z directions. Since a global method is used to describe the unknown, to perform a 3D transform (Fourier-Fourier-Chebyshev) the pencil must be reoriented along the three directions. The reorientation is performed through MPI-communications; this operation is required to compute of the non linear terms $\mathbf{S}$ and $\mathbf{S}_\phi$ (computed in the physical space). A schematic representation of the steps required to compute a 3D transform is shown in Figure 2.3.

2.4 Simulation Setup

The computational domain is a closed channel with dimensions $L_x \times L_y \times L_z = 4\pi h \times 2\pi h \times 2h$. Two different cases are considered: a single-phase reference case and a viscosity stratified case (lubricated channels). A viscosity ratio of $\lambda = 0.01$ (less viscous lubricating layer) is considered in the scope of this work. All simulations are performed at a constant single-phase power Reynolds number $Re_\Pi = 81050$ (i.e. constant pumping power). One should note at this point that for the lubricated case the equivalent power Reynolds number is $Re_\Pi = 50500$ (This is explained in detailed throughout Section 2.5). For the single-phase reference case, this corresponds approximately to a shear Reynolds number $Re_\tau \simeq 1000$ [13]. The magnitude of the surface tension of the liquid-liquid interface is set through the Weber number, $We_\Pi = 1250$ and corresponds to that of an oil/water interface [43]. The grid resolution has been chosen so to fulfill requirements imposed by DNS and at the same time to guarantee a proper resolution of the thin

interfacial layer (for the lubricated cases). For the single-phase reference case, a grid with the dicretization $N_x \times N_y \times N_z = 512 \times 512 \times 513$ was used, while for the lubricated channel case $N_x \times N_y \times N_z = 512 \times 256 \times 513$ cells were defined for the computational grid. The values of the Cahn and Péclet numbers are set to $Ch = 0.03$ and $Pe_\Pi = 7500$ respectively [17, 33]. An overview of the parameters used for the different cases is reported in Table 2.1.

For all simulations, the initial condition is taken from a preliminary DNS of single-phase fully developed turbulent channel flow at $Re_\tau = 1000$ which was performed using a constant pressure gradient (CPG) approach, and complemented by a proper definition of the initial distribution of the phase-field ϕ, so that the liquid-liquid interfaces are at the beginning flat and located at a distance $h_1 = \pm mh$ from the top and bottom walls (only for the lubricated channel case). Specifically, the initial condition used for the phase-field is

$$\phi(x, y, z) = \tanh\left(\frac{z - (1 - m)}{\sqrt{2}Ch}\right), \tag{2.81}$$

being m the thickness of the thin lubricating layer and z the wall-normal direction.

Results are reported using the CPI scaling system, which means that u_Π is used as reference velocity, h as reference length and h/u_Π as reference time. Note that angular brackets $\langle\cdot\rangle$ indicate average in space along the two homogeneous directions (x and y), while square brackets $[\cdot]$ indicate average in space (along the two homogeneous directions x and y) and in time.

In this work, the flow field is decomposed into a mean and a fluctuating part using a Reynolds decomposition: the mean component is a function of the wall-normal coordinate (z) and of time (t), while the fluctuating component depends on all the three spatial coordinates (x, y, z) and time (t). Therefore, for the velocity field one obtains:

$$u_i(x, y, z, t) = \underbrace{\langle u_i(z, t)\rangle}_{\text{Mean component}} + \underbrace{u_i'(x, y, z, t)}_{\text{Fluctuating component}}, \tag{2.82}$$

where $u_i(x, y, z, t)$ is the instantaneous flow field, $\langle u_i(z, t)\rangle$ the mean component averaged along x and y, and $u_i'(x, y, z, t)$ the fluctuating component. Similarly, the pressure field $p(x, y, z, t)$ (which do not include the mean pressure gradient contribution) is

System	λ	Re_Π	We_Π	Ch	Pe_Π	$N_x \times N_y \times N_z$
Single-phase	-	81050	-	-	-	$512 \times 512 \times 513$
Lubricated Channel	0.01	50500	1250	0.03	7500	$512 \times 256 \times 513$

Table 2.1 – Overview of the parameters used for the different examined cases. For a fixed single-phase power Reynolds number ($Re_\Pi = 81050$), we consider a single-phase reference case and a viscosity stratified case. The latter considers a viscosity ratio of $\lambda = 0.01$ (lubricating layers less viscous than the main layer). The surface tension of the multi-phase case is set via the Weber number. Please note that the grid requirements for the multi-phase case simulations are much larger than those of the single-phase case.

decomposed as follows:

$$p(x,y,z,t) = \underbrace{\langle p(z,t)\rangle}_{\text{Mean component}} + \underbrace{p'(x,y,z,t)}_{\text{Fluctuating component}} , \tag{2.83}$$

being $p(x,y,z,t)$ the instantaneous pressure field, $\langle p(z,t)\rangle$ the mean pressure and $p'(x,y,z,t)$ the pressure fluctuations.

2.5 Extension of the CPI Approach to Double Viscosity Stratified Multi-Phase Flows

The purpose of the following is to present the extension of the CPI approach to double viscosity stratified flows. Starting by briefly recapping its derivation for a single phase-phase flow. In particular, one would consider the flow inside a plane channel bounded by two walls located at $z = \pm h$ as shown in Figure 2.4 (a). The core fluid is characterized by a uniform viscosity η. A constant pumping power per unit area, P_p is used to drive the flow along the stream-wise direction. Assuming the flow laminar, the following velocity profile can be obtained:

$$u_x(z) = \frac{1}{2\eta}(p_x)\left(z^2 - h^2\right). \tag{2.84}$$

where (p_x) is the pressure gradient along the stream-wise direction. The bulk velocity (i.e. the average velocity across the channel section) can be computed integrating the

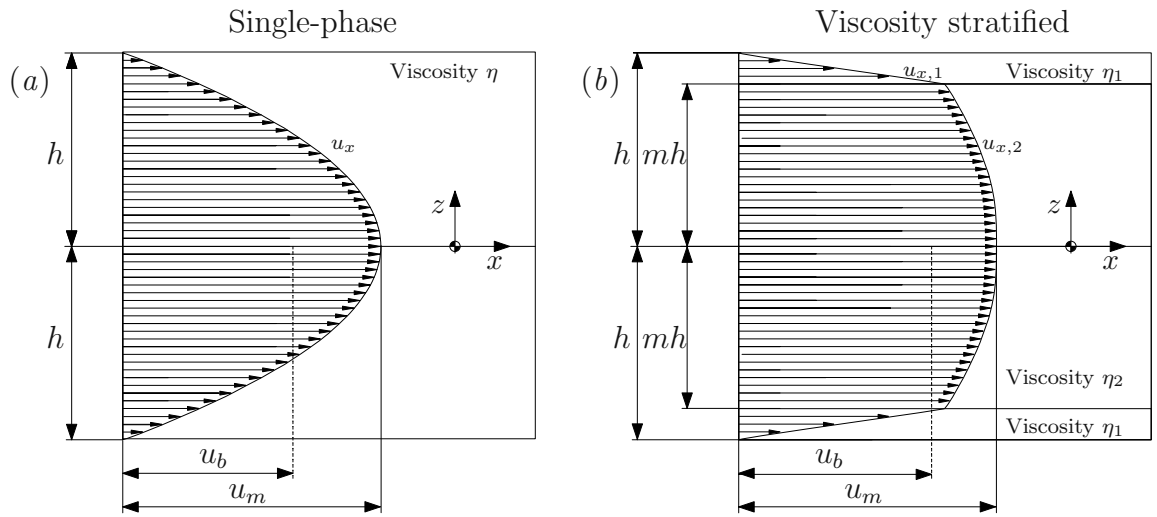

Figure 2.4 – Sketch of the channel configurations used to derive the laminar flow solution: single-phase (panel (a)) and viscosity stratified (panel (b)). For the single-phase, the viscosity, η, is uniform and thus a symmetric velocity profile, u_x, is obtained. For the viscosity stratified case, the thin lubricating layers at the top and bottom of the channel ($mh < z < h$ and $-mh > z > -h$) have viscosity η_1 while the primary layer ($-mh < z < mh$) has viscosity η_2. Again symmetric velocity profile ($u_{x,1}$ in the lubricating layer and $u_{x,2}$ in the primary layer) is obtained, due to the symmetry of the problem. For both panels, the maximum velocity, u_m, and the bulk velocity, u_b, have been highlighted.

velocity profile along the wall normal direction.

$$u_b = \frac{1}{2h}\int_{z=-h}^{z=h} u_x dz = \frac{1}{3\eta}\left(-p_x\right)h^2. \tag{2.85}$$

The power dissipated by the viscous forces can be computed as:

$$\epsilon = \frac{1}{2}\int_{z=-h}^{z=h}\eta\left(\frac{\mathrm{d}u_x}{\mathrm{d}z}\right)^2\mathrm{d}z = \frac{1}{\eta}\left(p_x\right)^2\frac{h^3}{3} = \frac{3\eta}{h}\underbrace{\left(p_x\right)^2\frac{h^4}{9\eta^2}}_{u_b^2} = \frac{3\eta u_b^2}{h}, \tag{2.86}$$

where the expression of the bulk velocity has been highlighted. At equilibrium (i.e. fully developed flow), the power dissipated by the viscous forces is equal to the power injected in the system. Matching the expression of P_p with Equation (2.86), one can quantify a velocity scale, u_Π, for the problem:

$$u_b = u_\Pi = u_\Pi^{sp} = \sqrt{\frac{P_p h}{3\eta}}. \tag{2.87}$$

To extend the CPI approach to double viscosity stratified flows, one can proceed in a similar fashion. One now considers a fully developed channel flow with three liquid layers on top of each other as shown in Figure 2.4 (b). Both top and bottom layers are characterized by viscosity η_1 and the middle (core) layer is characterized by viscosity η_2. The flow is laminar and the interfaces between the layers are located at $z = mh$ and $z = -mh$ (note that in the present work $m = 0.85$). No slip boundary conditions are applied at the top and bottom walls, while the continuity of velocity and viscous stresses is enforced at the interface [30, page 198]. The resulting velocity profile is:

$$u_x(z) = \begin{cases} u_{x,1} & \text{for } mh \leq z \leq h \\ u_{x,2} & \text{for } mh < z < -mh \\ u_{x,3} & \text{for } -mh \leq z \leq -h \end{cases} \tag{2.88}$$

Where $u_{x,1}$ and $u_{x,3}$ are the velocities of the top and bottom thin lubricating layers and $u_{x,2}$ is the velocity of the core fluid layer. Utilizing the geometric symmetry of this problem one can rewrite as follows:

$$u_x(z) = \begin{cases} u_{x,1} & \text{for } mh \leq z \leq h \\ u_{x,2} & \text{for } mh < z \leq 0 \end{cases} \tag{2.89}$$

and state the aforementioned velocities according to the definition of laminar plane channel velocity profiles as:

$$u_{x,1}(z) = \frac{1}{2\eta_1}(p_x)\left(z^2 - h^2\right), \tag{2.90}$$

$$u_{x,2}(z) = \frac{1}{2\eta_2}(p_x)\left(z^2 - Ah^2\right). \tag{2.91}$$

where the coefficient A, which depends on the thickness of the lubricating layer (i.e. on the parameter m) and on the viscosity ratio $\lambda = \eta_1/\eta_2$, is defined as;

$$A(\lambda, m) = \frac{1 - m^2(1 - \lambda)}{\lambda}, \tag{2.92}$$

The bulk velocity can be computed integrating the velocity profile along the wall-normal direction (i.e. the two velocity profiles over their corresponding thickness);

$$u_b = \frac{1}{h}\left(\int_{mh}^{h} u_{x,1}\left(z\right) dz + \int_{0}^{mh} u_{x,2}\left(z\right) dz\right), \tag{2.93}$$

which yields the following relation for the bulk velocity

$$u_b = -\frac{1}{3\eta_1}\left(-p_x\right) h^2 \underbrace{\left[\lambda m^3 + \left(1 - m^3\right)\right]}_{B}, \tag{2.94}$$

where the coefficient B has been introduced to highlight the main difference to the expression of the bulk-velocity of the single-phase flow as defined in Equation (2.94). Figure 2.5 illustrates the dependence of the geometry parameter on viscosity ratio and lubricating layer height. From a physical point of view, the ratio η_1/B can be interpreted as the equivalent viscosity of the system. The power dissipated by the viscous forces can be computed from the expression for the velocity profiles inserted into the equation for the dissipation

$$\epsilon = \int_{z=mh}^{z=h} \eta_1 \left(\frac{\mathrm{d}u_{x,1}}{\mathrm{d}z}\right)^2 \mathrm{d}z + \int_{z=0}^{z=mh} \eta_2 \left(\frac{\mathrm{d}u_{x,2}}{\mathrm{d}z}\right)^2 \mathrm{d}z. \tag{2.95}$$

After some algebra it is possible to obtain:

$$\epsilon = \int_{0}^{h} \eta\left(z\right) \left(\frac{du}{dz}\right)^2 dz \tag{2.96}$$

$$= \frac{1}{3\eta_1}\left(-p_x\right)^2 h^3 \left[\lambda m^3 + \left(1 - m^3\right)\right]^2. \tag{2.97}$$

As previously done for the single-phase flow case, one can highlight the expression for the bulk velocity

$$\epsilon = \frac{3\eta_1}{hB} \underbrace{\left(-p_x\right)^2 \frac{h^4}{9\eta_1^2} B^2}_{u_b^2}. \tag{2.98}$$

Consistently with the previous derivation, the bulk velocity is used as a reference velocity scale and its expression can be obtained by matching the expression of the

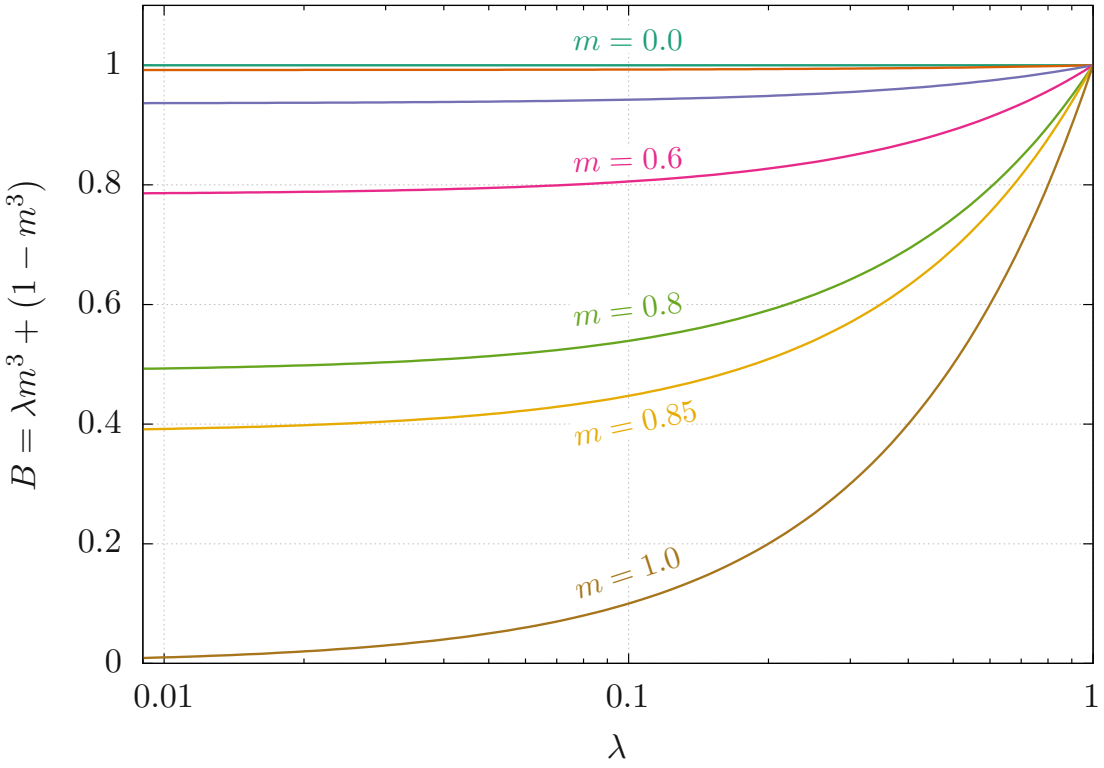

Figure 2.5 – Influence of viscosity ratio λ and core fluid fraction m on the geometry parameter B. The case studied in this work ($m = 0.85$) is marked by a yellow line (—).

viscous dissipation from Equation (2.98) with that of the pumping power. This gives:

$$u_\Pi = u_b = \sqrt{B\frac{P_p h}{3\eta_1}} = \sqrt{B}\underbrace{\sqrt{\frac{P_p h}{3\eta_1}}}_{u_\Pi^{sp}}. \tag{2.99}$$

Under CPI conditions, the coefficient $\sqrt{B}$ is used to account for the presence of a lubricating layer of different viscosity at the top and bottom walls (Equation (2.87)). Furthermore the equivalent Reynolds number of the multi-phase flow can be written as

$$Re_\Pi^{mp} = \frac{\rho u_\Pi^{mp} h}{\eta_1} = Re_\Pi^{sp}\sqrt{B}. \tag{2.100}$$

and the pressure gradient is obtained from

$$-p_x = \frac{3}{Re_\Pi B u_b}. \tag{2.101}$$

2.6 Details on the Implementation of the CPI Approach

The characteristic feature of the CPI approach is that the mean pressure gradient p_x driving the flow along the streamwise direction is updated every time step so to keep the power injected into the system constant (proportional to the product between the mean pressure gradient and the overall channel flow-rate). The mean pressure gradient at the new time step $n+1$ is obtained using a first-order accurate scheme [13]:

$$-{p_x}^{n+1} = \frac{3}{B Re_\Pi {u_b}^n}\,, \tag{2.102}$$

where u_b^n is the bulk velocity at the old time step n and B is the coefficient defined in Equation (2.94). The coefficient B has been introduced to re-scale the power Reynolds number to the equivalent system viscosity $\eta_1 B$. Indeed the power Reynolds number is computed using the viscosity of the lubricating layer η_1 as a reference, Equation (2.10). The bulk velocity is computed at each time-step as follows:

$$u_b^n = \frac{1}{2}\int_{z/h=-1}^{z/h=1} \langle u_x(z)\rangle dz\,, \tag{2.103}$$

where $\langle u_x(z)\rangle$ is the mean streamwise velocity profile. Such profile is obtained averaging the instantaneous streamwise velocity $u_x(x,y,z)$ along the two homogeneous directions (x and y) at the time step n.

3

Results

To better illustrate the physical behavior of the plane channel flows considered in this work, qualitative flow representations will be discussed. First appropriate flow metrics such as the mean pressure gradient, flow rates and velocity profiles will be utilized subsequently to quantify the differences. Lastly the turbulent kinetic energy (TKE) and mean kinetic energy (MKE) budgets including the energy-box representation [35] are discussed to investigate the influence of the presence of the lubricating layer as well as fluid-fluid interfaces on the flow dynamics. The energy-box method will first be applied to the whole channel domain (ensemble averaged) and to each phase separately (phase averaged) to describe the MKE and TKE fluxes between the core and lubricating phases [10, 38].

3.1 Qualitative Results

The first point of discussion will be to look at the flow structured in a statistically steady-state, after the initial transient behavior due to the initial conditions set for the field variables (velocity and phase) as well as the stream-wise pressure gradient, have been absorbed.

Figure 3.1 shows a map of the instantaneous stream-wise velocity on a streamwise section ($x - z$ plane) of the channel at $y = L_y/2$. Panel (a) represents the single-phase reference case as panel (b) shows the lubricated channel flow. The position of the interface ($\phi = 0$) is represented by a thin red line.

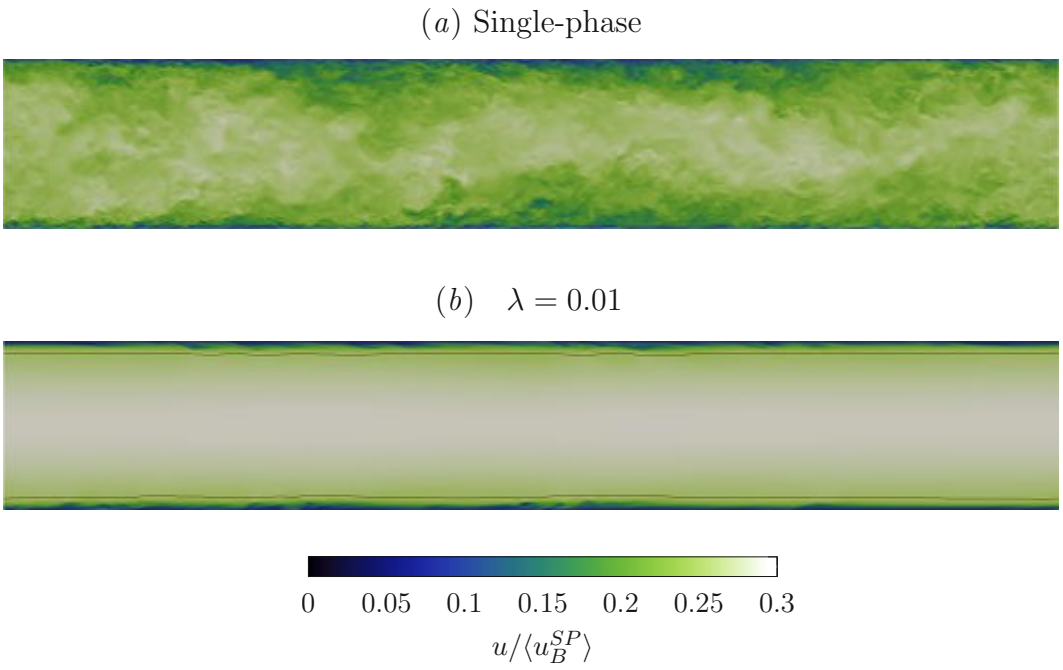

Figure 3.1 – Map of the instantaneous streamwise velocity in a cross section of the channel $(x-z)$. The single-phase case is shown in panel (a); the flow field of the multiphase case $\lambda = 0.01$ is shown in panel (b). For comparability the data is scaled to the power velocity of the single-phase reference flow. The instantaneous position of the interface is also visualized by a solid red line. The presence of the thin lubricating layers produce large flow modifications and lead to a stratified core flow.

The single-phase reference case shows the typical near-wall turbulence structures as expected for a fully turbulent flow in a channel as well as a fully turbulent core. On the other hand one can observe that for the lubricated case studied in this work, near the wall turbulent structures arise, but do not extend beyond the interface between the lubricating layers and the core flow. This is better appreciated in the close up view of Figure 3.2. Here one can clearly observe the lack of turbulent structures in the core of the lubricated case in contrast to the single phase case on the left.

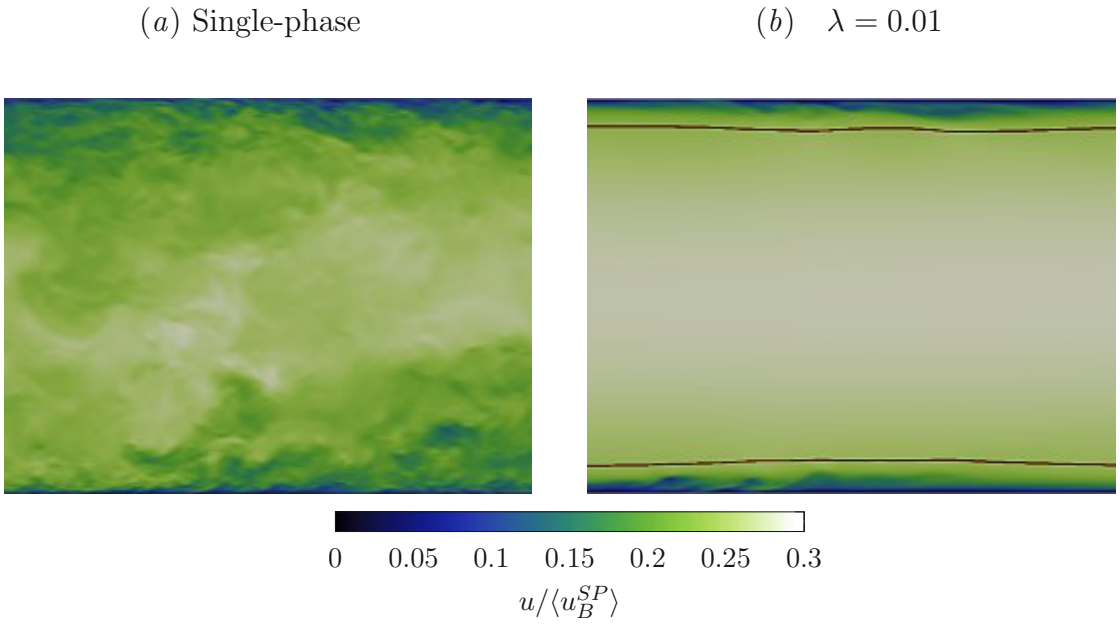

Figure 3.2 – Detail of the instantaneous streamwise velocity at the height of the upper interface ($z = 0.85$) in a cross section of the channel ($x - z$). The single-phase case is shown in panel (a); the flow field of the multiphase case $\lambda = 0.01$ is shown in panel (b). For comparability the data is scaled to the power velocity of the single-phase reference flow. The instantaneous position of the interface is also visualized by a solid red line. The presence of the thin lubricating layers produce large flow modifications and lead to a stratified core flow.

Figure 3.3 illustrates a map of the instantaneous turbulent kinetic energy ($u_i' u_i'/2$) on a cross section of the channel ($y - z$ plane) at $x = L_x/2$. Again the interface position is represented by a thin line on the panel of the multi-phase case (b). Panel (a) shows the single-phase reference flow with it's typical turbulent structures for a fully developed channel flow. In the case including the lubricating layers one can immediately identify that at both walls ($h = \pm 1$) near wall turbulence is generated, but due to the presence of the interface and the viscosity ratio λ the wall-normal transport of TKE is suppressed, leading to a laminar core flow, indicated by low magnitudes of TKE.

Further detail to the flow dynamics in the turbulent lubricating layer is presented in Figure 3.4. Both panels show the distribution of turbulent kinetic energy in a cross-section ($x - y$ plane) located inside the lubricating layer ($z = 0.95h$). In the single-phase reference case (panel (a)) one can observe the span wise periodic, stream wise velocity streaks typical for turbulent channel flow [9, 28, 39]. These structures are also present in the multi-phase flow (panel (b)), albeit one must notice the influence of

the interface nearby leads to a less homogeneous image of patch-wise laminar-turbulent structures.

Figure 3.5 illustrates the instantaneous interface position of the upper interface on the $x - y$ plane. One can see that the laminar patches of Figure 3.4 panel (b) correlate with areas in which the interface is characterized by a position closer to the wall indicated by white patches. Areas where the interface is positioned further from the wall the stream-wise turbulent streaks are stronger and similar to those observed in the single-phase case. Hence the existence of the laminar patches seem to originate from the deformation of the interface between lubricating and core flows. Locally the lubricating layer may be thin enough to suppress turbulence production. This reflects the results in previous work [37] where the near wall turbulence cycle can not be sustained as the lubricating layer is too thin (or the local Reynolds number is too small)[18–20].

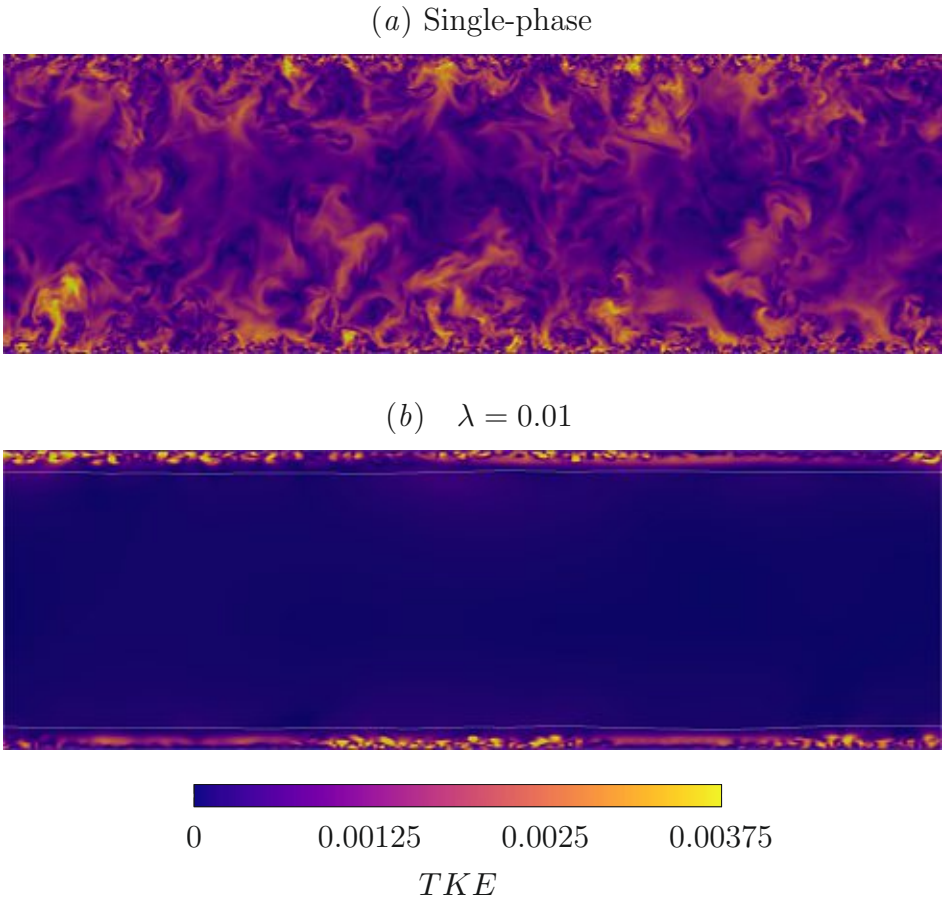

Figure 3.3 – Map of the instantaneous turbulent kinetic energy in a cross section of the channel $(y - z)$. The single-phase case is shown in panel (a); the flow field of the multi-phase case $\lambda = 0.01$ is shown in panel (b). The presence of the thin lubricating layers suppress the transport of turbulence to the core of the channel. The instantaneous interface position is highlighted with a thin white line.

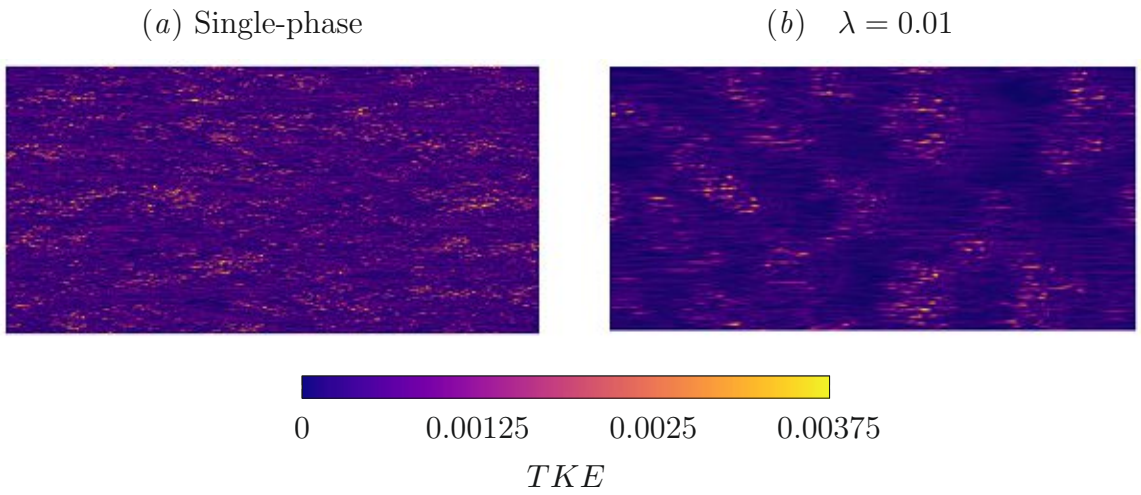

Figure 3.4 – Map of the instantaneous turbulent kinetic energy in a cross section of the channel $(x-y)$ at a cross section near the upper channel wall. The single-phase case is shown in panel (a); the turbulent kinetic energy of the multi-phase case $\lambda = 0.01$ is shown in panel (b).

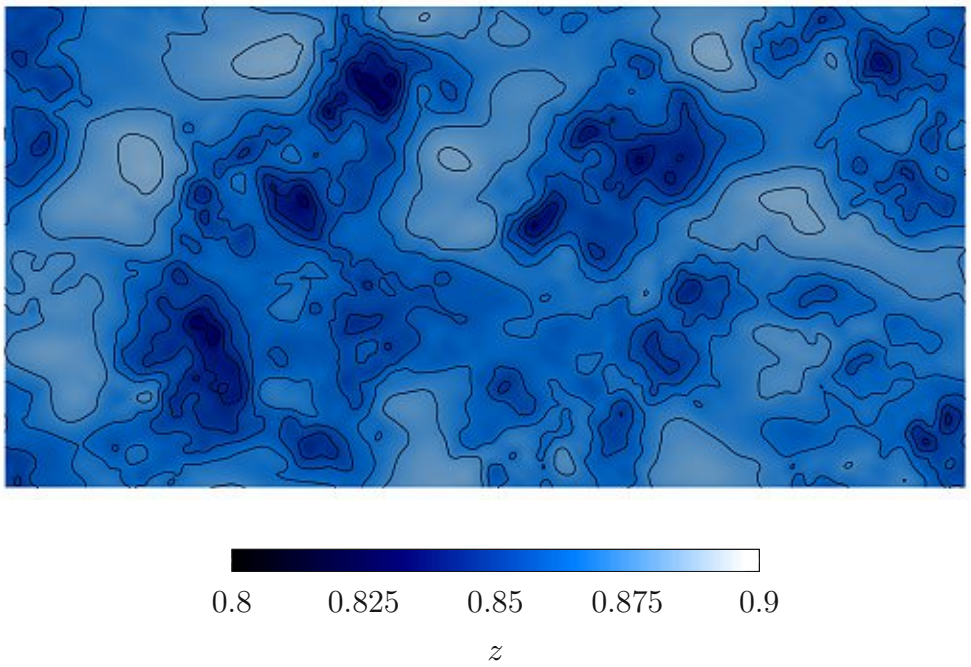

Figure 3.5 – Map of the instantaneous interface position in a cross section of the channel $(x-y)$ for the multi-phase case. Only the upper interface is displayed (nominal interface position $h = 0.85$). Iso-lines for the instantaneous interface position were added for clarity.

3.2 Flow Rates and Pressure Gradient

The effects of the qualitative changes in the flow physics can also be observed in the flow parameters. Focusing on the flow rate through the entire channel cross-section $[Q_t]$ and the mean stream-wise pressure gradient $[p_x]$, Figures 3.6 and 3.7 show the temporal behavior of these quantities. Due to the CPI approach an initial change of the pressure gradient and flow-rate can be seen, but as the simulation converges to a stead-state solution both flow rate and pressure gradient move toward a constant value for both the single-phase reference case and the multi-phase simulation. This is truncated from the images as their purpose is to show the statistically steady state the flow reaches and the interest of this work is in the magnitude of the variables.

Additionally one can calculate the time-averaged values of flow-rate through the entire channel cross-section $[Q_t]$, flow-rate through the primary core layer $[Q_2]$ of the lubricated case and the mean stream-wise pressure gradient $[p_x]$. These results are illustrated in Figure 3.8, with the green bars representing the increase of the flow parameters described above for the multi-phase simulation compared to the single-phase reference case. One can easily compare the cases considered in this work and see that the pressure gradient is reduced by 46 % and the total flow rate increases by 82 %, when the lubricating layers are introduced. A comparison of flow rates for the reference simulation and main fluid layer in the lubricated case yields an improvement of 63 %. This is the value of interest for engineering applications as one would be looking to improve the flow rate of the main fluid. By keeping the input power constant, due to the CPI approach, increasing flow rate as well as the smaller pressure gradient clearly hints towards a drag reduction. Note that for the sake of comparison the bulk flow rate as well as the pressure gradient are scaled to the single phase power velocity rather than the power velocity of the lubricated case. Details can be found in the derivation of section 2.5. One can find a summary of the results in Table 3.1

Case	$-p_x/p_{x_{lam}}$	$[Q_t]$
Single-phase	4.2	0.47
Multi-phase	2.3	0.86

Table 3.1 – Overview of the flow rates and pressure gradient results of the different examined cases.

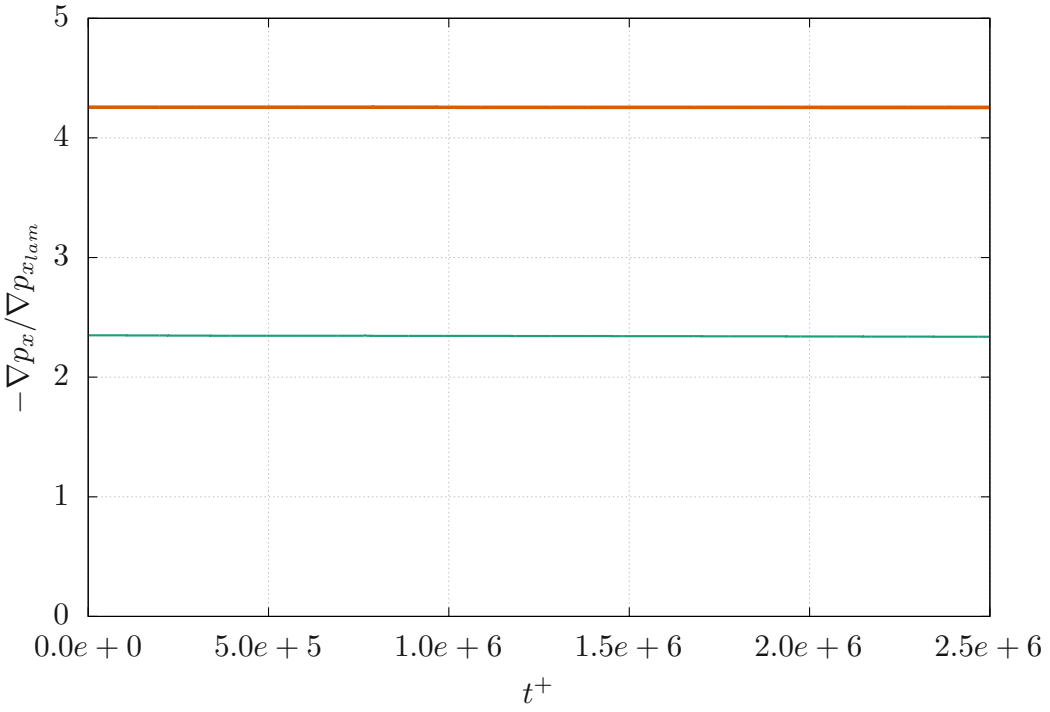

Figure 3.6 – Time evolution comparison of the stream-wise pressure gradient p_x for the lubricated channel (—) and the single-phase reference case (—). The data is normalized to the pressure gradient of a laminar channel flow at the same power Reynolds number and a bulk velocity $u_B = 1$.

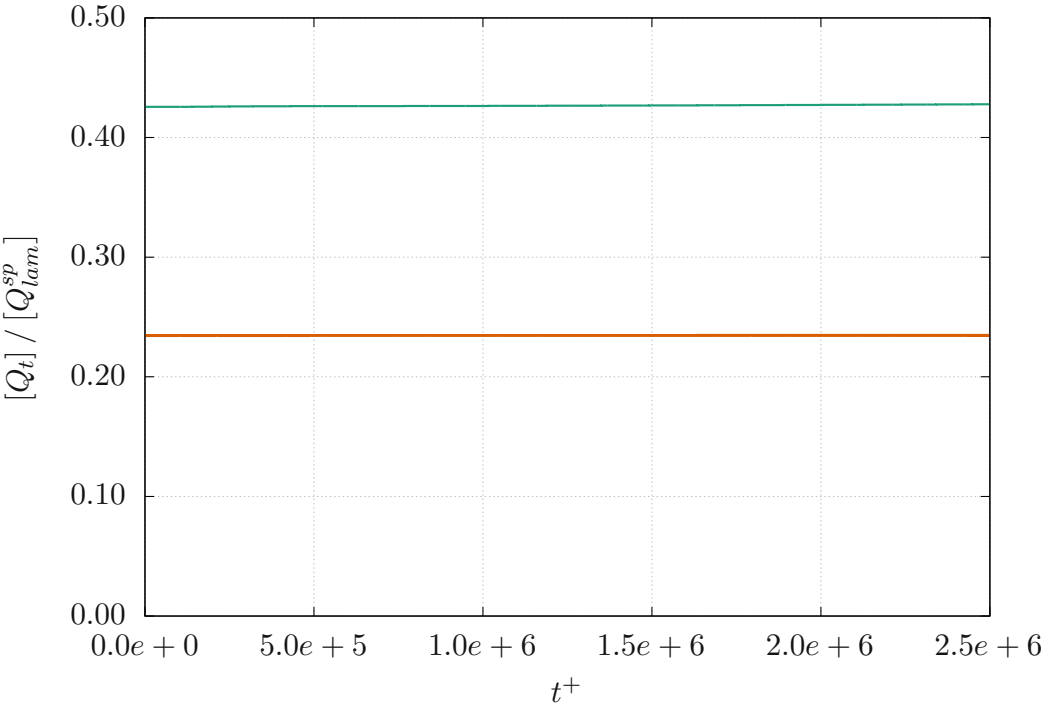

Figure 3.7 – Time evolution comparison of the bulk velocity for the lubricated channel (—) and the single-phase reference case (—).

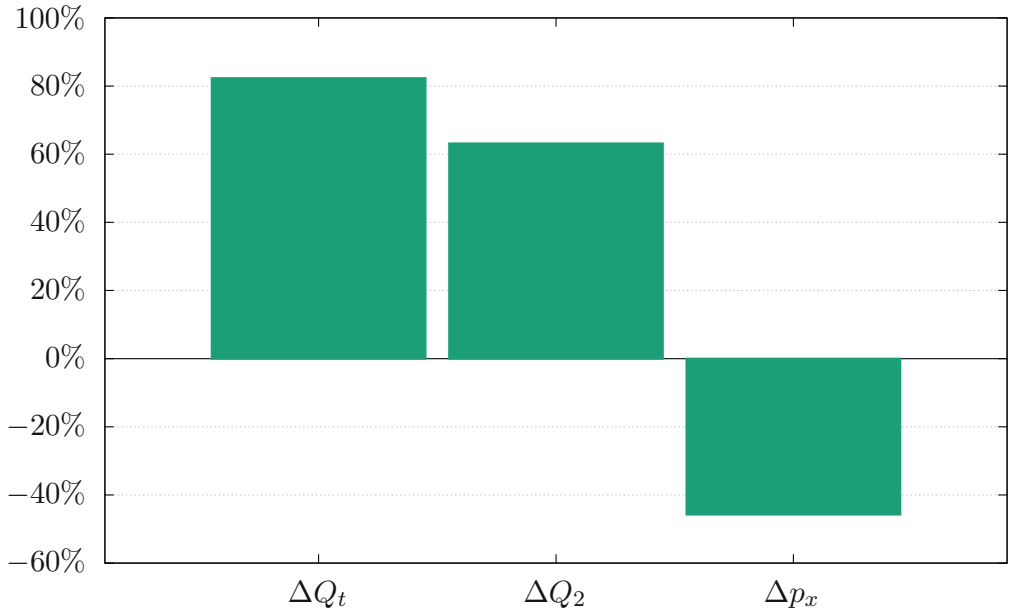

Figure 3.8 – Increase of the time-averaged values of flow-rate through the entire channel cross-section $[Q_t]$, flow-rate through the primary core layer $[Q_2]$ and the mean stream-wise pressure gradient $[p_x]$ of the lubricated channel in comparison with the single-phase reference case.

3.3 Velocity Profiles and Viscous Stresses

Similarly to the considerations regarding the average flow rates and pressure gradient it is necessary to analyze the time averaged streamwise velocity profiles, shown as a function of the wall normal coordinate in Figure 3.9. The nominal interface position ($z = \pm 0.85$) is marked by a gray vertical dash-dotted line. The single phase reference case is shown as an orange solid line and illustrates the typical properties of turbulent channel flow. Focusing on the multi-phase case, the introduction of the lubricating layers yields a symmetric distortion of the velocity profile. The streamwise velocity increases over the whole stretch of the channel core, with a visible decrease of the wall normal velocity gradient and a nearly parabolic evolution over the wall normal coordinate. Inside the lubricating layer, one can observe a stretching of the turbulent boundary layer in the presence of the interfacial forces.

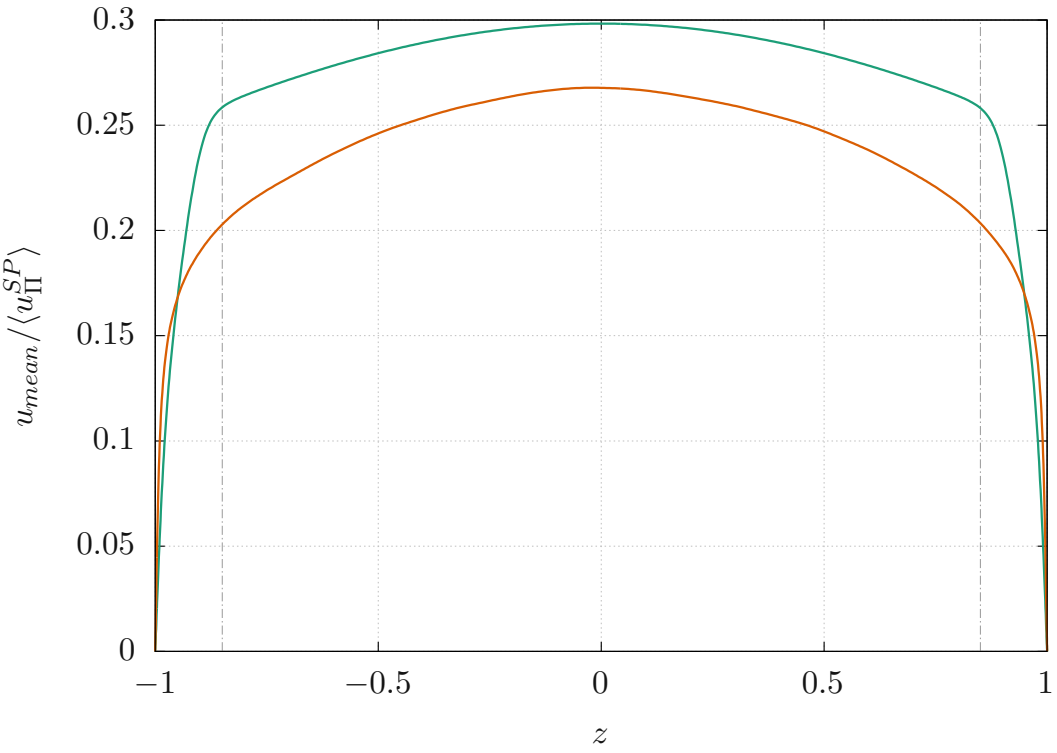

Figure 3.9 – Comparison of the mean streamwise velocity u component over the channel height z between the lubricated channel (——) and the single-phase reference case (——). The velocity components are averaged in spanwise and streamwise directions. Furthermore the data is scaled to the power-velocity of the single-phase reference flow $\langle u_\Pi^{SP}\rangle$. The nominal interface positions are marked with a gray dash-dotted line ($z = \pm 0.85$).

This influence can also be observed in Figure 3.10 where the viscous stresses are plotted as a function of the wall normal coordinate z. Again the single-phase reference case is presented as a solid orange line and the multi-phase case is illustrated by the means of a solid green line. After an initial decline in magnitude the viscous stresses increase approaching the nominal interface position, peaking in its immediate vicinity. This can be attributed to the influence of the surface tension at the liquid-liquid interface. The viscous stresses in the core of the channel show nearly linear behavior.

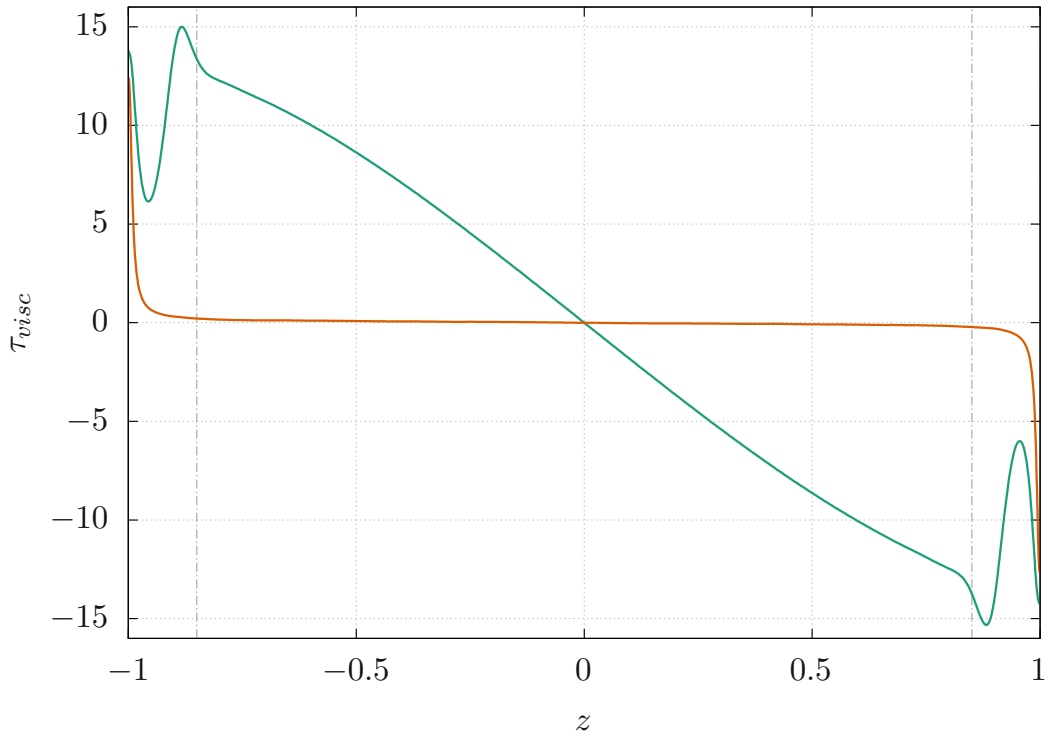

Figure 3.10 – Comparison of viscous stresses τ_{visc} over the channel height z between the lubricated channel (——) and the single-phase reference case (——). The shear stresses are averaged in span-wise and wall-normal directions. Furthermore the data is scaled to the power velocity of the single-phase reference flow $\langle u_{\Pi}^{SP} \rangle$. The nominal interface positions are marked with a gray dash-dotted line ($z = \pm 0.85$).

The comparison of the streamwise velocity fluctuations' root mean square (RMS) in Figure 3.11 can confirm the laminarization of the core in the lubricated case, drawn in green, as the magnitude of the RMS is orders of magnitude lower than the fully turbulent reference case shown as a solid orange line. Further one can identify two peaks inside the lubricating layer, the first resembling similar behavior to the single phase case and a second one closer to the nominal interface position illustrated by a vertical dash-dotted line. Plot of the spanwise and wall normal RMS of the velocity fluctuations show similar behavior qualitatively. Reduced magnitudes compared to the single phase reference case inside the lubricating layer are observed. This is most likely due to the laminar patches observed earlier in Figure 3.4. Approaching the nominal interface position one identifies a steep drop in RMS magnitudes in the core of the channel indicating laminarization, further cementing the observations of the previous sections.

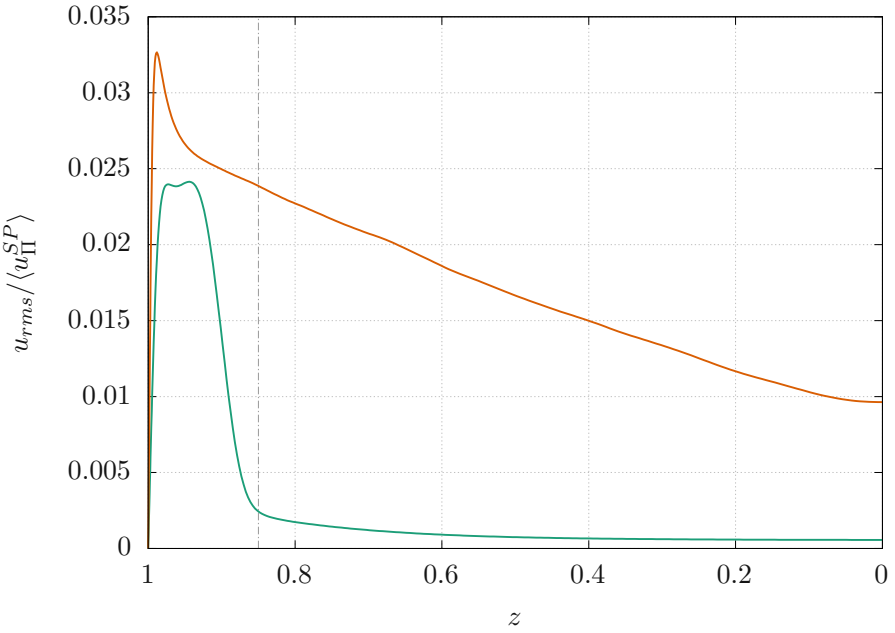

Figure 3.11 – Comparison of the streamwise velocity u_{rms} component RMS over the channel height z between the lubricated channel (—) and the single-phase reference case (—). The velocity component RMS are averaged in spanwise and streamwise directions. Furthermore the data is scaled to the power velocity of the single-phase reference flow $\langle u_\Pi^{SP}\rangle$. The nominal interface positions are marked with a gray dash-dotted line ($h = \pm 0.85$).

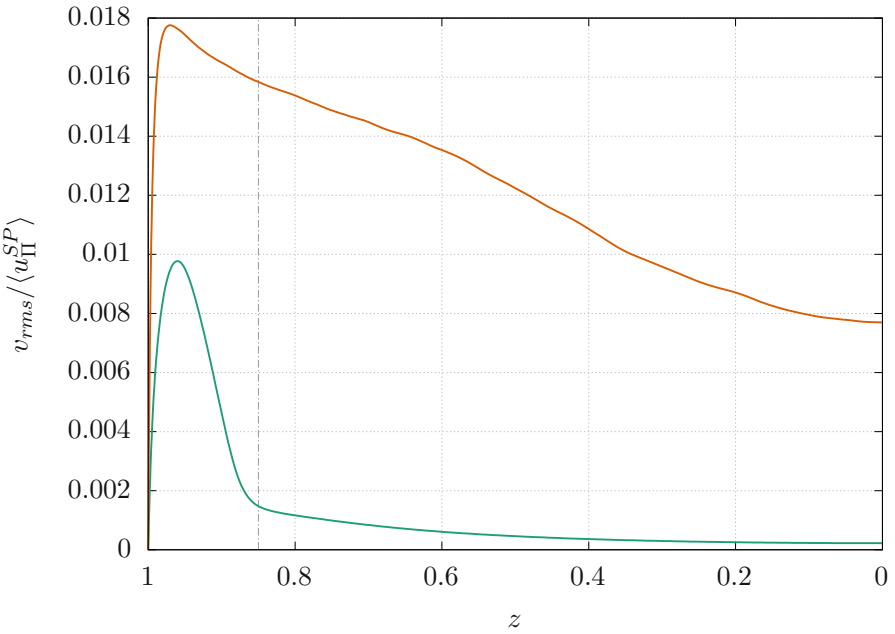

Figure 3.12 – Comparison of the spanwise velocity v_{rms} component RMS over the channel height z between the lubricated channel (—) and the single-phase reference case (—). The velocity component RMS are averaged in spanwise and streamwise directions. Furthermore the data is scaled to the power velocity of the single-phase reference flow $\langle u_\Pi^{SP}\rangle$. The nominal interface positions are marked with a gray dash-dotted line ($h = \pm 0.85$).

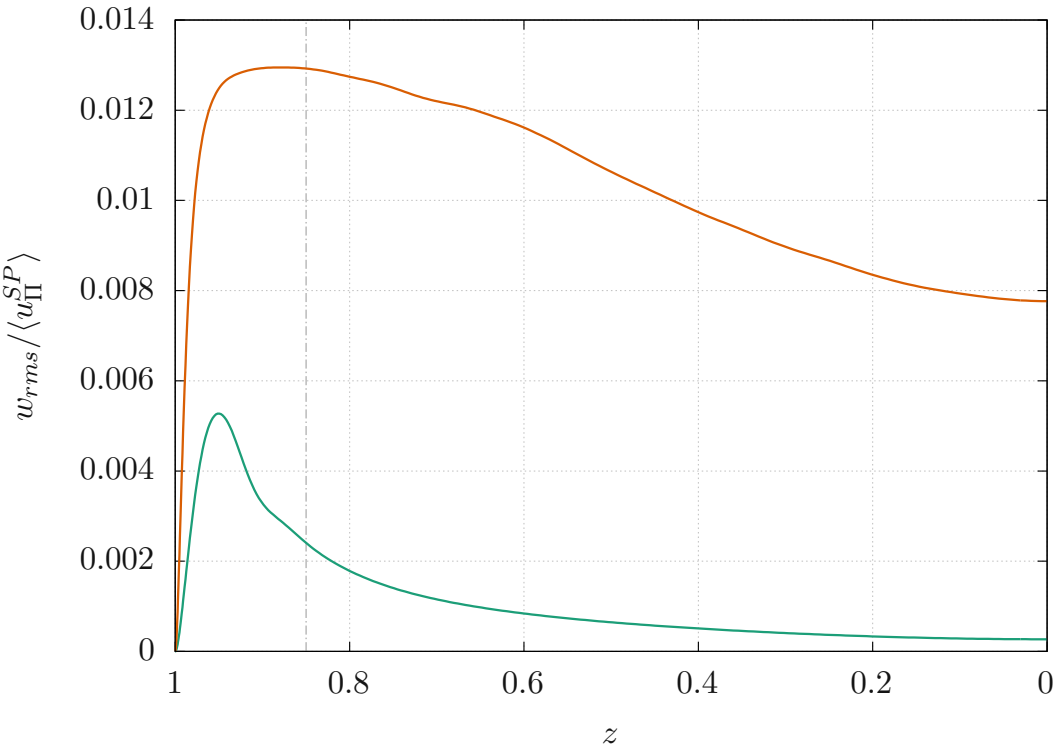

Figure 3.13 – Comparison of the wall-normal velocity w_{rms} component RMS over the channel height z between the lubricated channel (—) and the single-phase reference case (—). The velocity component RMS are averaged in spanwise and streamwise directions. Furthermore the data is scaled to the power velocity of the single-phase reference flow $\langle u_\Pi^{SP}\rangle$. The nominal interface positions are marked with a gray dash-dotted line ($h = \pm 0.85$).

3.4 Preliminary Concepts of the Energy-box Method

To describe the drag reduction mechanisms introduced by the presence of the thin lubricating layers at the top and bottom of the channel this work will utilize the framework of turbulent kinetic energy (TKE) and mean kinetic energy (MKE) boxes. [11, 35] This representation allows the illustration of the energy fluxes between the thin lubricating layers and the core fluid and subsequently study how they modify the flow regime in the channel. Utilizing the MKE and TKE balance equations, one can study how the energy injected into the system (by means of the mean pressure gradient) is transported and finally dissipated by viscous forces. Furthermore the effect on the transport of MKE and TKE between the lubricating and core layers can be visualized

and studied. As all simulations are performed at the same input power due to the implementation of the CPI method, the lubricated channel can be directly compared to the single-phase reference flow [11].

The first step is to split the total kinetic energy into the turbulent kinetic energy (TKE) and mean kinetic energy (MKE) components, dividing the flow into the kinetic energy linked to the velocity fluctuations and mean flow.

Both components of the total kinetic energy (MKE and TKE) can be expressed as follows:

$$\mathrm{MKE} = \frac{1}{2}\langle u_i \rangle \langle u_i \rangle \,, \tag{3.1}$$

$$\mathrm{TKE} = \frac{1}{2} u_i' u_i' \,, \tag{3.2}$$

with $\langle u_i \rangle$ describing the mean component of the velocity vector and u_i' as the fluctuations of the velocity vector (see Equation (2.83) for further information on the decomposition). Subsequently in this work the energy-box technique will be presented and applied to a single-phase reference case, followed by the extension to the double stratified lubricated channel.

3.4.1 Energy-box for the Single-Phase Flow

Starting from the Navier-Stokes equations the balance equations for the turbulent kinetic energy and mean kinetic energy are derived by multiplying with the velocity vector u and averaging the resulting equation (assuming a planar channel geometry). One then obtains an ensemble-averaged balance equation for the mean kinetic energy, [MKE] and fluctuating component of the kinetic energy, [TKE] [16, 26, 34].

For the ensemble-averaged [MKE], the resulting transport equation for the single phase reference flow is:

$$\begin{aligned} \frac{D\,[\mathrm{MKE}]}{Dt} = & \underbrace{\left[\langle u_i' u_j' \rangle \frac{\partial \langle u_i \rangle}{\partial x_j}\right]}_{P_k} \underbrace{- \left[\langle u_i \rangle \langle p_x \rangle\right]}_{\Pi_m} - \underbrace{\left[\frac{\partial (\langle u_i' u_j' \rangle \langle u_i \rangle)}{\partial x_j}\right]}_{T_m} \\ & + \underbrace{\left[\frac{1}{2 Re_\Pi} \frac{\partial}{\partial x_j}\left(\langle \eta(\phi) \rangle \frac{\partial \langle u_i \rangle^2}{\partial x_j}\right)\right]}_{D_m} \underbrace{- \left[\frac{\langle \eta(\phi) \rangle}{Re_\Pi} \frac{\partial \langle u_i \rangle}{\partial x_j} \frac{\partial \langle u_i \rangle}{\partial x_j}\right]}_{\epsilon_m} , \end{aligned} \tag{3.3}$$

the term on the left hand side describes the material rate of change in [MKE]. For the study present it is zero, as the simulations are analyzed at a steady-state. Looking at the terms on the right hand side of Equation (3.3) represent the rate of turbulent kinetic energy production by the mean flow P_k, the power injected in the system through the mean pressure gradient Π_m, the transport work performed by the Reynolds stresses T_m, the viscous diffusion of mean kinetic energy D_m and the mean flow viscous dissipation ϵ_m.

The same can be done for the ensemble-averaged [TKE] and one will obtain the following equation:

$$\begin{aligned}\frac{D\,[\mathrm{TKE}]}{Dt} = &- \underbrace{\left[\langle u_i' u_j' \rangle \frac{\partial \langle u_i \rangle}{\partial x_j}\right]}_{P_k} - \underbrace{\left[\frac{\partial \langle p' u_i' \rangle}{\partial x_i}\right]}_{\Pi_k} - \underbrace{\left[\frac{1}{2}\frac{\partial \langle u_i' u_i' u_j' \rangle}{\partial x_j}\right]}_{T_k} \\ &+ \underbrace{\left[\frac{1}{2Re_\Pi}\frac{\partial}{\partial x_j}\left(\eta(\phi)\frac{\partial \langle u_i' u_i' \rangle}{\partial x_j}\right)\right]}_{D_k} - \underbrace{\left[\frac{\eta(\phi)}{Re_\Pi}\frac{\partial u_i'}{\partial x_j}\frac{\partial u_i'}{\partial x_j}\right]}_{\epsilon_k}\end{aligned} \tag{3.4}$$

as discussed above the term on the left hand side represents the material rate if change in [TKE] and is identified to be zero as the steady-state solution of the simulations are considered in this work. The right hand side of Equation (3.3) can be divided into the following terms: the rate of turbulent kinetic energy production by the mean flow P_k, the pressure diffusion Π_k, the turbulent diffusion T_k, the viscous diffusion of turbulent kinetic energy D_k and the turbulent dissipation ϵ_k. To better visualize the role of the individual terms one should first analyze them in a canonical single-phase flow [16, 34]. For this case all terms linked to the surface tension disappear and the terms including the viscosity map $\eta(\phi)$, namely the viscous diffusion (D_m and D_k) and the viscous dissipation (ϵ_m and ϵ_k) are simplified due to uniform and constant viscosity. Hence viscous diffusion of the mean kinetic energy (D_m) and of the turbulent kinetic energy (D_k) can be written as:

$$D_m = \left[\frac{1}{2Re_\Pi}\frac{\partial^2 \langle u_i \rangle^2}{\partial x_j^2}\right], \tag{3.5}$$

$$D_k = \left[\frac{1}{2Re_\Pi}\frac{\partial^2 \langle u_i' u_i' \rangle}{\partial x_j^2}\right], \tag{3.6}$$

while the expression for the mean flow viscous dissipation (ϵ_m) and for the turbulent dissipation (ϵ_k) are:

$$\epsilon_m = -\left[\frac{1}{Re_\Pi}\frac{\partial\langle u_i\rangle}{\partial x_j}\frac{\partial\langle u_i\rangle}{\partial x_j}\right], \tag{3.7}$$

$$\epsilon_k = -\left[\frac{1}{Re_\Pi}\frac{\partial u_i'}{\partial x_j}\frac{\partial u_i'}{\partial x_j}\right]. \tag{3.8}$$

Starting with the [MKE] balance equation, the left side is zero as the scope of this work is restricted to analyzing the fully developed steady-state channel flow. The right hand side of Equation (3.3) consists of one source term namely the input power (Π_m) via the mean pressure gradient. Due to the CPI approach and steady-state flow it is constant over time. The mean flow viscous dissipation (ϵ_m) and the generation of [TKE] by the production term (P_k) are responsible for the dissipation of the power injected into the system hence acting as sinks in Equation (3.3). This leaves us with the transport work performed by the Reynolds stresses (T_m) and the viscous diffusion of the mean flow kinetic energy (D_m). These terms exclusively redistribute [MKE] across the channel and therefore do not show up in the overall balance.

The same can be done for the [TKE] balance equation. Again the left hand side is identified as zero due to the steady-state. On the right hand side there is one source term in the form of the [TKE] production (P_k) describing the amount of power used to generate turbulent velocity fluctuations. As kinetic energy from the mean flow is redistributed to the turbulent velocity fluctuations the term is present in Equation (3.4) with the opposite sign with respect to Equation (3.3). Following the pattern of the [MKE] balance equation one can identify one sink in the form of the turbulent dissipation (ϵ_k) leaving us with transport terms redistributing [TKE] across the channel. These are identified as the pressure diffusion (Π_k), the turbulent diffusion (T_k) and the viscous diffusion of the turbulent kinetic energy (D_k) and do not contribute to the overall balance of [TKE] in the system.

To visualize the relative contributions of the terms in the [MKE] and [TKE] balance equations it is beneficial to integrate the individual terms along the wall-normal direction considering the quantities have been averaged in time and along the homogeneous directions:

$$\overline{A_{m/k}} = \int_{z/h=-1}^{z/h=+1} A_{m/k}\,dz\,, \tag{3.9}$$

$A_{m/k}$ describing a generic term appearing in the [MKE] or [TKE] balance equations and $\overline{A_{m/k}}$ the integral of such quantity along the wall-normal direction (from the bottom to the top wall). This leads to the following classification of the integrated terms:

- $\overline{A_{m/k}} > 0$: the term is a source of power in the [MKE] or [TKE] balance equation.
- $\overline{A_{m/k}} = 0$: the term does not have an active role (i.e. internal transport).
- $\overline{A_{m/k}} < 0$: the term is a sink of power in the [MKE] or [TKE] balance equation.

After the integration step, the [MKE] and [TKE] balance equations can be rewritten as two macroscopic balance equations of the system, for the [MKE] the following relation can be found:

$$+\overline{P_k} + \overline{\Pi_m} + \overline{\epsilon_m} = 0\,, \tag{3.10}$$

while for the [TKE] one obtains:

$$-\overline{P_k} + \overline{\epsilon_k} = 0\,. \tag{3.11}$$

The sum of these equations reported above leads to a power balance equation for the entire system:

$$\overline{\Pi_m} + \overline{\epsilon_m} + \overline{\epsilon_k} = 0\,, \tag{3.12}$$

which states that all the power injected in the system via the mean pressure gradient is dissipated by the viscous forces. A part of the viscous dissipation is linked to the mean flow ($\overline{\epsilon_m}$) and the remainder is linked to the turbulent motion ($\overline{\epsilon_k}$).
Utilizing this information one can construct the energy-box for the flows studied in this work. These are best explained looking at Figure 3.14 in which illustration the energy-box for the single-phase reference case is provided. The rectangle on the left side represents the macroscopic balance for the [MKE], Equation (3.10) and the one on the right the macroscopic balance for the [TKE], Equation (3.11). Sinks and sources are denoted via the colored arrows, with such colored in green pointing into the boxes illustrating sources, arrows in blue stretching from one box to the next describing energy exchange. Red arrows pointing outwards showing sinks for the respective macroscopic balance equation. The magnitudes of the individual terms are reported next to the corresponding arrow and are normalized by the input power from the mean pressure

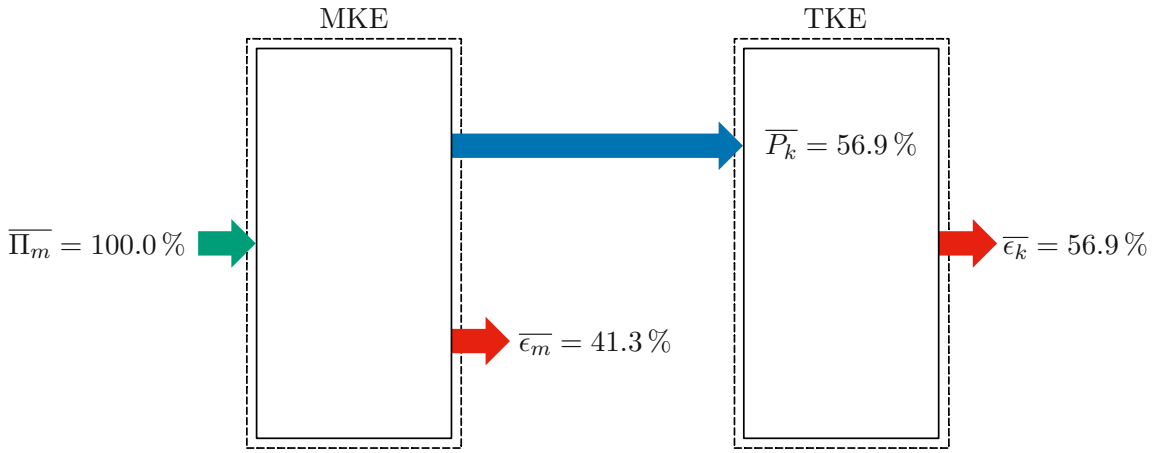

Figure 3.14 – Energy-box representation for the single-phase reference case. The left box represents the mean kinetic energy (MKE) of the flow, while the right box identifies turbulent kinetic energy (TKE) of the flow. Each arrow refers to a different energy flux, whose magnitude is normalized by the value of the power input. The power injected in the system, $\overline{\Pi_m}$, is represented by a green arrow; the mean flow viscous dissipation, $\overline{\epsilon_m}$, by a red arrow (left) and the TKE production, $\overline{P_k}$, by a blue arrow. Finally, the turbulent dissipation, $\overline{\epsilon_k}$, is represented by a red arrow (right).

work $\overline{\Pi_m}$ of each respective case. As discussed the sole source of [MKE] on the left is the mean pressure work $\overline{\Pi_k}$ and injected into the system. In the present case $\simeq 41.1\,\%$ of the input is dissipated by the mean flow $\overline{\epsilon_m}$ (red arrow) while the remainder ($\simeq 56\,\%$) contributes to the production of turbulent kinetic energy $\overline{P_k}$, depicted via the blue arrow.

Moving on to the [TKE] box on the right, one can identify the production of [TKE] $\overline{P_k}$ as a source term transferring power from the mean flow to the turbulent velocity fluctuations. This is dissipated solely by the turbulent dissipation $\overline{\epsilon_m}$.

Putting the whole system together conveniently visualizes the information extracted from Equation (3.12). Specifically, all the power injected via the mean pressure gradient (green arrow) is dissipated by the mean flow and turbulent dissipation (left and right bottom red arrows).

3.4.2 Energy-box for the Lubricated Channel

Proceeding to the multi-phase flow, the same theory can be applied to study the influence of the lubricating layers on the energy fluxes inside the lubricated channel flow. Extending the energy-box representation to the case of a lubricated channel, one will again obtain energy balance equations by multiplying the Navier-Stokes equations

by the mean and fluctuating velocity field and averaging the resulting equations in space and time. For the [MKE], one arrives at:

$$\frac{D\,[\mathrm{MKE}]}{Dt} = \underbrace{\left[\langle u_i' u_j' \rangle \frac{\partial \langle u_i \rangle}{\partial x_j}\right]}_{P_k} \underbrace{- \left[\langle u_i \rangle \langle p_x \rangle\right]}_{\Pi_m} - \underbrace{\left[\frac{\partial (\langle u_i' u_j' \rangle \langle u_i \rangle)}{\partial x_j}\right]}_{T_m}$$
$$+ \underbrace{\left[\frac{1}{2Re_\Pi}\frac{\partial}{\partial x_j}\left(\langle \eta(\phi) \rangle \frac{\partial \langle u_i \rangle^2}{\partial x_j}\right)\right]}_{D_m} \underbrace{- \left[\frac{\langle \eta(\phi) \rangle}{Re_\Pi}\frac{\partial \langle u_i \rangle}{\partial x_j}\frac{\partial \langle u_i \rangle}{\partial x_j}\right]}_{\epsilon_m} + \underbrace{\left[\langle u_i \rangle \frac{3}{\sqrt{8}}\frac{Ch}{We_\Pi}\frac{\partial \tau_{ij}^c}{\partial x_j}\right]}_{\psi_m}, \quad (3.13)$$

And for the [TKE]:

$$\frac{D\,[\mathrm{TKE}]}{Dt} = - \underbrace{\left[\langle u_i' u_j' \rangle \frac{\partial \langle u_i \rangle}{\partial x_j}\right]}_{P_k} \underbrace{- \left[\frac{\partial \langle p' u_i' \rangle}{\partial x_i}\right]}_{\Pi_k} \underbrace{- \left[\frac{1}{2}\frac{\partial \langle u_i' u_i' u_j' \rangle}{\partial x_j}\right]}_{T_k}$$
$$+ \underbrace{\left[\frac{1}{2Re_\Pi}\frac{\partial}{\partial x_j}\left(\eta(\phi)\frac{\partial \langle u_i' u_i' \rangle}{\partial x_j}\right)\right]}_{D_k} \underbrace{- \left[\frac{\eta(\phi)}{Re_\Pi}\frac{\partial u_i'}{\partial x_j}\frac{\partial u_i'}{\partial x_j}\right]}_{\epsilon_k} + \underbrace{\left[u_i' \frac{3}{\sqrt{8}}\frac{Ch}{We_\Pi}\frac{\partial \tau_{ij}^c}{\partial x_j}\right]}_{\psi_k} \quad (3.14)$$

In the scope of this work the equations consider matched densities but different viscosities of the fluid layers in the channel. The latter is achieved with the term $\eta(\phi)$ representing the dimensionless viscosity map of the system (see also Equation (2.7)). This must be included in the viscous diffusion (D_m and D_k) and the viscous dissipation (ϵ_m and ϵ_k). Further the surface tension terms appear defined as ψ_m which describes the work of the surface tension forces on the mean flow, and ψ_k representing work exchanged via the surface tension forces, between the interface and the fluctuating field [31].

A further note on the surface tension must be made in regard to the computational grid. Looking at the expression for power exerted by the surface tension forces [21, p. 242] under the assumption of constant and uniform surface tension (i.e. $d\sigma/dt = 0$ and $\nabla_s \sigma = \mathbf{0}$) are written as follows [3, 10, 21]:

$$\frac{1}{We}\frac{dA}{dt} = -\int_A u_i f_i^\sigma dA\,, \quad (3.15)$$

Integrating the i-th component of the velocity vector (u_i) times the i-th component of the surface tension forces (f_i^σ) over the total interfacial area (A) (Equation (3.15)) one can see that an increase of the interfacial area (i.e. an increase of the interfacial energy) comes with a negative work of the surface tension forces as velocity and surface tension

forces have opposite sign. Rewriting the terms above with respect to the computational grid, accounting for the finite thickness of the interface layer in this model a volume integral can be written for Equation (3.15).

$$\frac{1}{We}\frac{dA}{dt} = -\int_A u_i f_i^\sigma dA\,, = -\int_V u_i \underbrace{\frac{3}{\sqrt{8}}\frac{Ch}{We}\frac{\partial \tau_{ij}^c}{\partial x_j}}_{\text{Surface tension forces}} dV\,, \tag{3.16}$$

where τ_{ij}^c is the Korteweg tensor. Rewriting the right hand side and averaging in time one derives:

$$\frac{1}{We}\left[\frac{dA}{dt}\right] = -L_x L_y \int_{z/h=-1}^{z/h=+1}\left[u_i \frac{3}{\sqrt{8}}\frac{Ch}{We}\frac{\partial \tau_{ij}^c}{\partial x_i}\right] dz\,. \tag{3.17}$$

Referencing to the steady-state analysis the interfacial area is constant ($[dA/dt] = 0$) and after decomposition into mean and fluctuating contributions one obtains:

$$\underbrace{\int_{z/h=-1}^{z/h=+1}\left[\langle u_i\rangle \frac{3}{\sqrt{8}}\frac{Ch}{We}\frac{\partial \tau_{ij}^c}{\partial x_j}\right] dz}_{\overline{\psi_m}} + \underbrace{\int_{z/h=-1}^{z/h=+1}\left[u_i' \frac{3}{\sqrt{8}}\frac{Ch}{We}\frac{\partial \tau_{ij}^c}{\partial x_j}\right] dz}_{\overline{\psi_k}} = 0\,, \tag{3.18}$$

Hence looking at Equation (3.18), one can see that the total power of the surface tension forces (i.e. interfacial contributions $\overline{\psi_m}$ and $\overline{\psi_k}$) is zero [10, 21]:

$$\overline{\psi_m} = \overline{\psi_k} \tag{3.19}$$

Equation (3.19) highlights the pure elastic behavior of the interface and thus the absence of net energy dissipation associated with its deformation. Macroscopic [MKE] balance equation for the multi-phase system can be written as:

$$\overline{P_k} + \overline{\Pi_m} + \overline{\epsilon_m} + \overline{\psi_m} = 0\,, \tag{3.20}$$

while for the [TKE] one derives:

$$-\overline{P_k} + \overline{\epsilon_k} + \overline{\psi_k} = 0\,. \tag{3.21}$$

Summing these two equations and using Equation (3.18), one obtains a power balance equation for the entire system:

$$\overline{\Pi_m} + \overline{\epsilon_m} + \overline{\epsilon_k} = 0\,, \tag{3.22}$$

Therefore the surface tension forces transfer power between [MKE] and [TKE]. It is important to state that due to spreading out the interface to a finite thickness, the contributions of the mean flow and fluctuating velocity components do not match ($|\overline{\psi_m}| \geq |\overline{\psi_k}|$). Albeit the differences found in this work were never larger than $\simeq 0.5\,\%$ of the total input power into the system. The energy box of the multi-phase case ($\lambda = 0.01$) is shown in Figure 3.15. As previously defined the [MKE] and [TKE] budget contributions are reported next to the corresponding color-coded arrow and normalized by the input power (Π_m). The interface contribution is illustrated with a yellow arrow transferring power from the [MKE] box to [TKE] box with an intermediate box representing the interface and its dynamics - an elastic component absorbing and releasing energy.

Compared to the single-phase case in Figure 3.14 the mean flow dissipation $\overline{\epsilon_m}$ increases to 83.6 % while the [TKE] production reduces to 19.0 %. Accordingly, and considering that the contribution of the interfacial term ψ_m, is small (0.4 %), the turbulent dissipation $\overline{\epsilon_m}$ decreases to 19 %. This indicates a drag reduction as it is usually associated to an increase of $\overline{\epsilon_m}$ and a decrease of $\overline{\epsilon_k}$ [11].

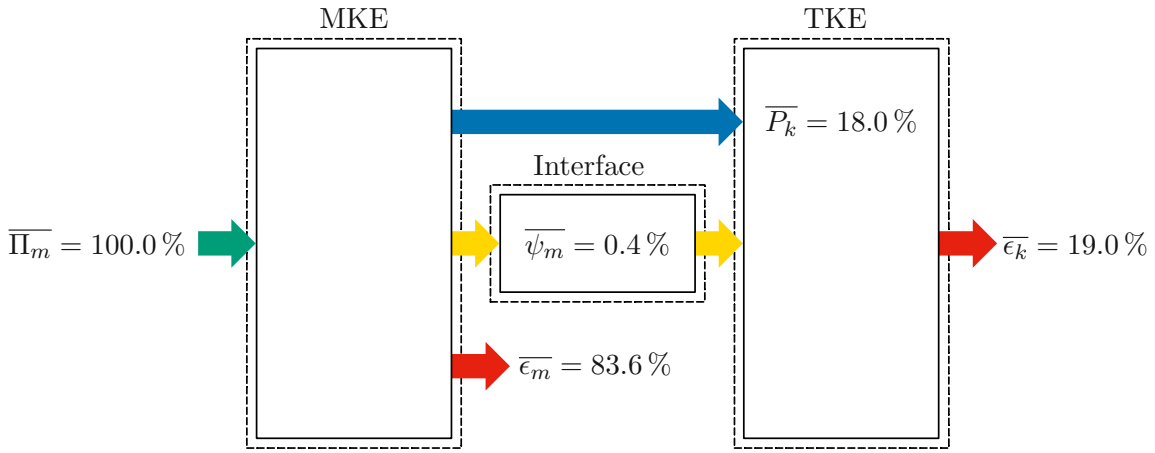

Figure 3.15 – Ensemble-averaged energy-box for the case of the lubricated channel at $\lambda = 0.01$. The left box represents the MKE of the flow while the right box identifies the TKE of the flow. The power injected in the system, $\overline{\Pi_m}$, is represented using a green arrow. The mean flow viscous dissipation, $\overline{\epsilon_m}$, is identified by a red arrow (bottom left); the TKE production term, $\overline{P_k}$, and the surface tension contribution, $\overline{\psi_m}$, are represented with a blue and a yellow arrow, respectively. Finally, the turbulent dissipation, $\overline{\epsilon_k}$, is represented using a red arrow (right).

3.5 Virtually-Lubricated Channel

To fully understand the phase-averaged energy boxes we first derive a virtually-lubricated energy box for the single-phase reference case. This allows one to compare the results of the phase-averaged multi-phase case with single-phase data which is ideally separated into the lubricating and core layers at the nominal interface position (i.e. at a distance $0.15h$ from the top and bottom walls). Figure 3.16 illustrates the virtually-lubricated channel for the present reference case. Again conformation to the color coding defined earlier is sustained, illustrating the power input with a green arrow. Here it is divided into a contribution of the virtual lubricating layer (denoted by index 1) and virtual core flow (denoted by index 2) respectively. Utilizing the symmetric properties of the problem in this work, the virtual lubricating layer box may be shown as the sum of upper and lower contributions. Consistent with all energy boxes in this work the [TKE] production is represented by a blue arrow. MKE as well as TKE dissipation are shown via a red arrow and the transport fluxes (transport/redistribution terms) between the layers are identified by dark blue arrows. These have previously identified to be zero but this only holds true when integrating over the entire system domain. From the data presented in Figure 3.16 it is obvious that a significant fraction of the viscous

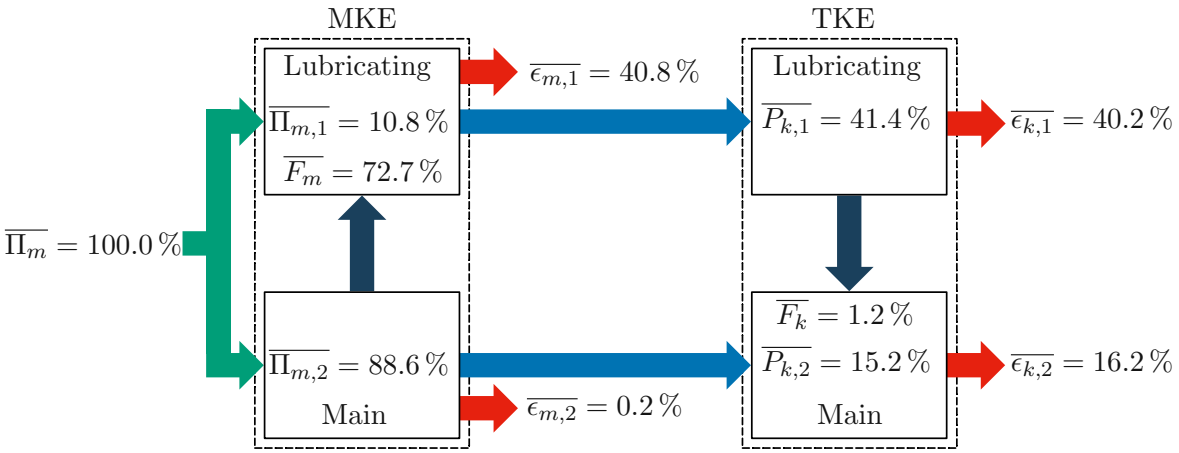

Figure 3.16 – Energy-box for the virtually-lubricated channel, i.e. a single-phase case virtually separated into the lubricating and main layers. The virtual separation is located at the nominal position of the interfaces (i.e. at distance $0.15h$ from top and bottom wall). The left dashed box represents the MKE of the flow while the right box identifies TKE of the flow. Inside each dashed box, the top and bottom rectangles identify the (virtual) lubricating and main layers, respectively. Each arrow represents a different energy flux, whose magnitude is reported (near the arrow) normalized by the power input value. With respect to previous energy-boxes, an additional subscript is used to distinguish between the lubricating and main layer contributions. The power injected in the system, $\overline{\Pi_m}$, is represented with a green arrow; the mean flow viscous dissipations, $\overline{\epsilon_{m,1}}$ and $\overline{\epsilon_{m,2}}$, with red arrows (left) and the TKE production terms, $\overline{P_{k,1}}$ and $\overline{P_{k,2}}$, with blue arrows. Finally, the turbulent dissipations, $\overline{\epsilon_{k,1}}$ and $\overline{\epsilon_{k,2}}$, are represented with red arrows (right). Note the appearance of dark blue arrows, identifying energy fluxes exchanged between the main and lubricating layers, $\overline{F_m}$ and $\overline{F_k}$.

dissipation of the TKE ($\overline{\epsilon_{m,1}}$ and $\overline{\epsilon_{m,2}}$) and MKE ($\overline{\epsilon_{k,1}}$ and $\overline{\epsilon_{k,2}}$) is contributed by the lubricating layer. This could be due to the fully turbulent flow regime shrinking the near-wall turbulence closer to the boundary and thus containing the dissipation inside the lubricating layer. The representation in Figure 3.16 gives a better understanding of the energy transferred and dissipated in the region virtually corresponding to the primary layer of the channel, and favors the introduction of an energy transfer efficiency, which can be conveniently defined as:

$$\mathcal{H}_{sp} = \frac{\overline{\epsilon_{m,2}}}{\overline{\epsilon_{m,2}} + \overline{\epsilon_{k,2}}} = 0.013 \tag{3.23}$$

illustrating the ratio between the energy dissipated by the mean flow velocity, and the maximum theoretical energy contained in the virtual core layer (after considering the energy transferred from the main layer to the lubricating layer and vice versa). Further references to the energy transfer efficiency will be made in the following section.

3.6 Phase Averaged Energy Boxes

In the following a procedure is presented to better separate the amount of power dissipated in either the lubricating layers and core flow compared to the ensemble averaged energy box. The representation discussed in Section 3.4.2 does not provide separation between the contributions of the lubricating layers and the primary core flow. More importantly information about the fluxes between the layers is completely hidden from analysis due to the averaging procedure being applied to the entire volume of the channel. To improve on this insufficiency one can compute the balance equations for each liquid layer and derive a more elaborate energy box [10, 38]. This is expected to solidify the previous observations and provide additional insight by describing the energy fluxes between the different layers. The first step is to define a local concentration ($0 \leq c_l \leq 1$) utilizing the phase-field variable ϕ:

$$c_1 = \frac{\phi + 1}{2}\,, \qquad c_2 = \frac{1 - \phi}{2}\,, \tag{3.24}$$

with c_1 defining the local concentration of the lubricating fluid and c_2 that of the core layer. By simply multiplying the [MKE] and [TKE] balance equations Equation (3.14) and (3.13) with the terms in 3.24 accordingly. one receives a description for the individual layers and it is possible to derive kinetic energy balance equations as described in previous sections. Introducing an additional subscript l to identify the each layer the [MKE] balance equations for the two liquid layers become (in shortened notation):

$$\frac{D\,[\mathrm{MKE}]_l}{Dt} = P_{k,l} + \Pi_{m,l} + T_{m,l} + D_{m,l} + \epsilon_{m,l} + \psi_{m,l}\,, \tag{3.25}$$

while the [TKE] balance equations are written as:

$$\frac{D\,[\mathrm{TKE}]_l}{Dt} = -P_{k,l} + \Pi_{k,l} + T_{k,l} + D_{k,l} + \epsilon_{k,l} + \psi_{k,l}\,, \tag{3.26}$$

In terms of physics, the contributions of the terms in Equation (3.25) and Equation (3.26) still correlate to the descriptions derived in the previous sections. However, the different contributions are now specific for the layer they are related to. As an example $\Pi_{k,1}$ is the power introduced to the system due to pressure occurring in the lubricating

layers, while $\Pi_{k,2}$ is the power introduced via the primary layer. The left hand side can be considered zero due to the steady state nature of the problem discussed in this work. Computing the integral of the different terms along the wall-normal direction and utilizing the notation in previous sections the [MKE] balance equations are:

$$\overline{P_{k,1}} + \overline{\Pi_{m,1}} + \overline{T_{m,1}} + \overline{D_{m,1}} + \overline{\epsilon_{m,1}} + \overline{\psi_{m,1}} = 0\,, \tag{3.27}$$

for the lubricating layer and:

$$\overline{P_{k,2}} + \overline{\Pi_{m,2}} + \overline{T_{m,2}} + \overline{D_{m,2}} + \overline{\epsilon_{m,2}} + \overline{\psi_{m,2}} = 0\,, \tag{3.28}$$

for the main layer.

Compared to Equation (3.20) the integrals of the work performed by the Reynolds stress ($T_{m,l}$) and of the viscous diffusion of the mean flow kinetic energy ($D_{m,l}$) do not equal zero anymore as only the contribution of part of the domain is accounted for [10, 38]. Albeit the sum of the two equations and utilizing mass conservation ($c_1 + c_2 = 1$), the mentioned terms cancel out and the combined balance equation reads:

$$\underbrace{\overline{P_{k,1}} + \overline{P_{k,2}}}_{\overline{P_k}} + \underbrace{\overline{\Pi_{m,1}} + \overline{\Pi_{m,2}}}_{\overline{\Pi_m}} + \underbrace{\overline{\epsilon_{m,1}} + \overline{\epsilon_{m,2}}}_{\overline{\epsilon_m}} + \underbrace{\overline{\psi_{m,1}} + \overline{\psi_{m,2}}}_{\overline{\psi_m}} = 0\,. \tag{3.29}$$

The sum of the contributions from the two phases (e.g. $\overline{P_{k,1}} + \overline{P_{k,2}}$) is the overall contribution ($\overline{P_k}$) and thus, the macroscopic balance Equation (3.20) can be obtained. Similarly, for Equation (3.26), after integration, the [TKE] balance equations are:

$$-\overline{P_{k,1}} + \overline{\Pi_{k,1}} + \overline{T_{k,1}} + \overline{D_{k,1}} + \overline{\epsilon_{k,1}} + \overline{\psi_{k,1}} = 0\,, \tag{3.30}$$

for the lubricating layer and

$$-\overline{P_{k,2}} + \overline{\Pi_{k,2}} + \overline{T_{k,2}} + \overline{D_{k,2}} + \overline{\epsilon_{k,2}} + \overline{\psi_{k,2}} = 0\,, \tag{3.31}$$

for the main layer.

Also for the two [TKE] balance equations, the integrals of pressure diffusion ($\overline{\Pi_{k,2}}$), turbulent diffusion ($T_{k,l}$) and viscous diffusion of the turbulent kinetic energy ($D_{m,l}$)

are not zero anymore.

However, when one sums the two equations, the contributions of the two above mentioned terms cancel out and the result is:

$$\underbrace{-\overline{P_{k,1}} - \overline{P_{k,2}}}_{-\overline{P_k}} + \underbrace{\overline{\epsilon_{k,1}} + \overline{\epsilon_{k,2}}}_{\overline{\epsilon_k}} + \underbrace{\overline{\psi_{k,1}} + \overline{\psi_{k,2}}}_{\overline{\psi_k}} = 0\,, \tag{3.32}$$

which is the macroscopic balance Equation (3.21).

The summary of the discussion above is illustrated in Figure 3.17 referring to the multi-phase case considered in this work. Recalling the convention in the previous energy-box representations. The dashed rectangle on the left illustrates the [MKE] balance equation, while the right dashed rectangle shows the [TKE] balance equation. Contributions of the surface tension are displayed by the dashed rectangle in the center with the according fluxes represented utilizing yellow arrows. The power input is divided into a contribution injected into the lubricating layer and a part induced into the core flow, shown as green arrows. The mean flow and turbulent dissipation of each layer are represented by red arrows, while the [TKE] production terms are represented by blue arrows. In this representation one introduces arrows to illustrate the mean and turbulent kinetic energy fluxes between the phases colored dark-blue [10, 38]. For the [MKE] box (left) this arrow specifically represents the work done by the Reynolds stresses and the [MKE] viscous diffusion summarized into the quantity $\overline{F_m}$, while for the [TKE] box (right) one accounts for pressure, viscous and turbulent diffusion identified by the quantity $\overline{F_k}$.

The energy fluxes in Figure 3.17 cannot be compared to the values observed in canonical single-phase turbulent channel flow, since the flows are characterized by different volumes. However one can conveniently compare to the values of the virtually lubricated channel as the conceptual framework in which the virtual (primary and lubricating) layers are characterized by the same nominal volume as the actual layers in the lubricated channel. As expected from the problem geometry most of the energy input into the channel is attributed to the core layer ($\simeq 90\,\%$), while only a small fraction of the total input is directed to the lubricating layer ($\simeq 10\,\%$). Progressing to the top of the image one can single out the lubricating layer and analyze it on its own. The main portion of the mean flow energy dissipation is due to the lubricating layer ($\simeq 54\,\%$). A considerable amount

of energy is still contributing to the production of turbulence in the lubricating layer ($\simeq 17\,\%$) which is in contrast to the core layer, where there is very little production of [TKE] in the core ($\simeq 0.2\,\%$) indicating laminarization of the flow. The turbulent kinetic energy of the lubricating layer is almost completely dissipated with little [TKE] flux $\overline{F_k}$ to the main layer ($\simeq 1\,\%$). It is interesting to note that albeit most of the energy is input into the core layer, only ($\simeq 10\,\%$) of the total energy is dissipated there as well. This is illustrated in the [MKE] box on the left where approximately $70\,\%$ of the total energy is transported to the lubricating layer via work done by the Reynolds stresses and the [MKE] viscous diffusion. Again the contribution of the interfacial layer is rather small ($\simeq 0.3\,\%$). Finally one must notice a discrepancy between the input power and the total viscous dissipation in the channel. A deficit of approximately $18\,\%$ can be observed. This reveals a weakness of the numerical setup in the present work. As discussed in Section 3.4 in steady-state flow one would expect the power input to balance the dissipation. This is the case for the isolated [TKE] budget but the source of the deficit can be found in the [MKE] budget. This is attributed to the fact that the transition in viscosity is spread over a distance of multiple grid cells, hence the extent of the modeled interface is expanded to a length larger than the Kolmogorov scale in wall-normal direction. This issue is amplified in the lubricating layer due to the high local Reynolds number and the low viscosity ratio λ.

An interpretation of the results achieved can only be in junction with the conclusions drawn from the virtually lubricated single-phase case discussed in Section 3.4.2. Coming back to the efficiency parameter defined earlier $\mathcal{H} = \overline{\epsilon_{m,2}}/\overline{\epsilon_{m,2}} + \overline{\epsilon_{k,2}}$, one would obtain $\mathcal{H}_{mp} = 0.87$ for the lubricated case presented in this work. Put into relation to the single-phase case $\mathcal{H}_{mp}/\mathcal{H}_{sp} = 0.87/0.013 \simeq 67$ one can observe a significant DR due to the combined effect of laminarization in the core layer and lower viscosity in the lubricating layer.

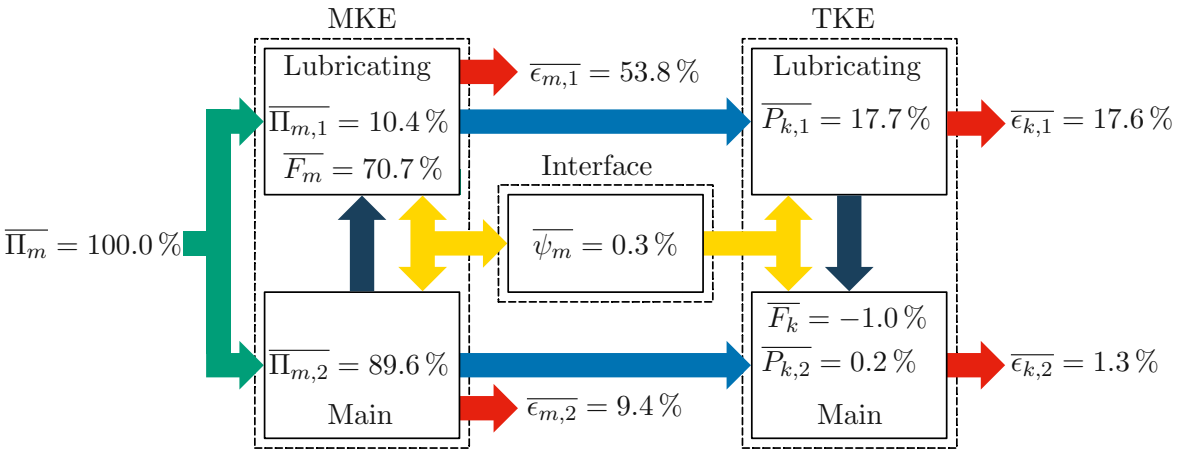

Figure 3.17 – Phase-averaged energy-boxes for the lubricated channel: $\lambda = 0.01$ The left dashed box represents the MKE of the flow while the right one represents the TKE of the flow. Inside each dashed box, the top and bottom rectangles identify the lubricating and main layer, respectively. The power injected in the system, $\overline{\Pi_m}$, is represented by a green arrow. The mean flow viscous dissipation, $\overline{\epsilon_{m,1}}$ and $\overline{\epsilon_{m,2}}$, and turbulent dissipation, $\overline{\epsilon_{k,1}}$ and $\overline{\epsilon_{k,2}}$, are represented by red arrows while the TKE production terms, $\overline{P_{k,1}}$ and $\overline{P_{k,2}}$, by blue arrows. Finally, surface tension contribution, $\overline{\psi_m}$, is represented by a yellow arrow. The dark blue arrows linking lubricating and main layer boxes (inside each dashed box) represent the energy fluxes of MKE and TKE between the two layers, $\overline{F_m}$ and $\overline{F_k}$, respectively.

3.7 Theoretical Prediction of the Drag Reduction

Before the focus is turned to drawing conclusions in respect to the results presented above, it is useful to investigate a simplified theoretical approach to predict the effect of the lubricating layers on the drag reduction performance. In this case one can consider the following equation [37].

$$h_1^+ = h_1 \frac{Re_\tau}{\lambda}, \tag{3.33}$$

here h_1 is the thickness of the lubricating layer in outer units, Re_τ the equivalent shear Reynolds number (in the case presented in this work it equates to 1000) and λ is the viscosity ratio. One can now compare the result from Equation (3.33) with the minimum value necessary to generate a self-sustained near-wall turbulence cycle ($h_{1,min}^+ \simeq 60\ w.u.$ [19, 20]), one can predict the flow regime in the lubricating layer and acquire further information on the drag reduction mechanisms in the present work. For the lubricated channel in this study $h_1^+ > 60\ w.u.$ which is consistent with the observations made in Section 3.1. Hence the main drag reduction mechanism for the lubricated channel can be identified as the viscosity difference between the two fluids. On further note the

larger inertial forces associated with larger Reynolds numbers can lead to the breakage of the thin lubricating layer and consequently a loss in drag reduction performance. By decreasing the lubricating layer height h_1 or reducing the Reynolds number one can expect a partial laminarization of the lubricating layer which leads to improved drag reduction performance [1, 2]. Decreasing the lubricating layer height is in principle a good strategy to improve drag reduction performance but this has some drawbacks since the waves generated at the liquid/liquid interface could reach the channel walls, therefore disrupting the lubricating layer and its drag reduction properties.

4

Conclusion

In the scope of this work direct numerical simulation was utilized to analyze the possibility of drag reduction via lubricating layers in a plane channel. Accomplished by the injection of a thin lubricating layer into the top and bottom near wall regions of the channel, one can favor the transportation of the primary core fluid.

The focus here was laid on examining the possibility of core laminarization in the case of large viscosity ratios ($\lambda = 0.01$) compared to a single-phase reference flow. A phase field-method (PFM) has been used to describe the dynamics of the interface, which is characterized by a uniform value of the surface tension. Furthermore an important aspect of the study is the use of the constant power input (CPI) approach to perform the simulations. The CPI approach offers a well-defined theoretical framework for the analysis of the different DR techniques since the obtained results are not anymore influenced by the amount of power injected into the flow.

The present results show that a significant drag reduction can be achieved in the lubricated channel case. In the case of $\lambda = 0.01$ drag reduction of 63 % could be achieved. This is a clear indication of the role the viscosity ratio plays when trying to maximize drag reduction. Albeit one cannot neglect the effect of the surface tension, hindering the transfer of turbulent kinetic energy between the turbulent lubricating layer to the laminarized core flow. So although the lubricating layer is turbulent following the increased local Reynolds number, the core remains laminar due to the elastic surface tension element in the form of the liquid-liquid interface. It has been shown in literature that the introduction of an elasticity factor inside a flow – for example, polymers or wall elasticity – can induce DR [44]. However, and differently from previous investigations, in present work, the elasticity is concentrated in deformable surfaces inside the channel. Further investigations into the DR mechanisms have been conducted by looking at the

mean kinetic energy and turbulent kinetic energy budgets. Introducing a graphical representation by the means of the energy-box method, energy fluxes were examined first in single-phase reference channel and later extended to the multi-phase case by utilizing the phase averaging technique. This has given detailed insight into the mechanism responsible for drag reduction on a quantitative basis.

By introducing an energy transfer efficiency parameter $\mathcal{H}$ it was possible to quantify the ratio between mean and total energy dissipation in the primary core fluid layer. Values greater than one ($\mathcal{H}/\mathcal{H}_{sp} > 1$) clearly indicate a drag reduction which is in agreement with the findings in this work.

Future research will focus on increasing the resolution of the multi-phase simulation. Issues with the numerical stability of the lubricated channel DNS have led to requiring an undesirable increase of the Cahn number and resulting in the turbulent structures inside the lubricating layers being slightly underresolved. This also leads to an increase in the extent of the viscosity transition in the volume near the liquid-liquid interface and is suspected to be the main attributor to the [MKE] budget imbalance. Improving these aspects of the DNS simulation would also allow the examination of vorticity transport mechanisms as well as parameter sweeps such as variations of the nominal lubricating layer thickness or the viscosity ratio between the core and lubricating fluids. Assessing their effects on the formation of turbulence in the lubricating layers.

Bibliography

[1] S. Ahmadi, A. Roccon, F. Zonta, and A. Soldati. Turbulent drag reduction by a near wall surface tension active interface. *Flow, Turbul. Combust.*, 100(4):979–993, 2018.

[2] S. Ahmadi, A. Roccon, F. Zonta, and A. Soldati. Turbulent drag reduction in channel flow with viscosity stratified fluids. *Comput. Fluids*, 176:260–265, 2018.

[3] R. Aris. *Vectors, Tensors and the Basic Equations of Fluid Mechanics*. Dover Publications, 1989.

[4] U.M. Ascher, S.J. Ruuth, and B.T.R. Wetton. Implicit-explicit methods for time-dependent partial differential equations. *SIAM J. Numer. Anal.*, 32(3):797–823, 1995.

[5] V.E. Badalassi, H.D. Ceniceros, and S. Banerjee. Computation of multiphase systems with phase field models. *J. Comput. Phys*, 190(2):371–397, 2003.

[6] R. Bai, K. Chen, and D.D. Joseph. Lubricated pipelining: stability of core-annular flow. Part 5. Experiments and comparison with theory. *J. Fluid Mech.*, 240:97–132, 1992.

[7] J. P. Boyd. *Chebyshev and Fourier spectral methods*. Courier Dover Publications, 2001.

[8] K. Chen, R. Bai, and D.D. Joseph. Lubricated pipelining. Part 3 Stability of core-annular flow in vertical pipes. *J. Fluid Mech.*, 214:251–286, 1990.

[9] S.I. Chernyshenko and M.F. Baig. The mechanism of streak formation in near-wall turbulence. *J. Fluid Mech.*, 544:99–131, 2005.

[10] M.S. Dodd and A. Ferrante. On the interaction of Taylor length scale size droplets and isotropic turbulence. *J. Fluid Mech.*, 806:356–412, 2016.

[11] D. Gatti, A. Cimarelli, Y. Hasegawa, B. Frohnapfel, and M. Quadrio. Global energy fluxes in turbulent channels with flow control. *J. Fluid Mech.*, 857:345–373, 2018.

[12] S. Ghosh, T.K. Mandal, and P.K. Das. Review of oil water core annular flow. *Renew. Sust. Energy Rev.*, 13:1957–1965, 2009.

[13] Y. Hasegawa, M. Quadrio, and B. Frohnapfel. Numerical simulation of turbulent duct flows with constant power input. *J. Fluid Mech.*, 750:191–209, 2014.

[14] H.H. Hu, T. S. Lundgren, and D.D. Joseph. Stability of core-annular flow with a small viscosity ratio. *Phys. Fluids*, 2(11):1945–1954, 1990.

[15] J.D. Isaac and J.B. Speed. Method of piping fluids, 1904. US Patent 759,374.

[16] K. Iwamoto, Suzuki Y., and N. Kasagi. Reynolds number effect on wall turbulence: toward effective feedback control. *Int. J. Heat Fluid Fl.*, 23(5):678 – 689, 2002.

[17] D. Jacqmin. Calculation of Two-Phase Navier–Stokes Flows Using Phase-Field Modelling. *J. Comput. Phys*, 155(1):96–127, 1999.

[18] J. Jiménez. Near-wall turbulence. *Phys. Fluids*, 25:101302, 2013.

[19] J. Jiménez and P. Moin. The minimal flow unit in near-wall turbulence. *J. Fluid Mech.*, 225:213–240, 1991.

[20] J. Jiménez and A. Pinelli. The autonomous cycle of near-wall turbulence. *J Fluid Mech.*, 389:335–359, 1999.

[21] D.D. Joseph. *Stability of Fluid Motions: II.* Springer-Verlag, 1976.

[22] D.D. Joseph and Y.Y. Renardy. *Fundamentals of Two-fluid Dynamics: Lubricated transport, drops, and miscible liquids.* 1993.

[23] D.D. Joseph, M. Renardy, and Y. Renardy. Instability of the flow of two immiscible liquids with different viscosities in a pipe. *J. Fluid Mech.*, 141:309–317, 1984.

[24] D.D. Joseph, R. Bai, K.P. Chen, and Y.Y. Renardy. Core-annular flows. *Annu. Rev. Fluid Mech.*, 29(1):65–90, 1997.

[25] T.W. Kao and C. Park. Experimental investigations of the stability of channel flows. part 2. two-layered co-current flow in a rectangular channel. *J. Fluid Mech.*, 52(3):401–423, 1972.

[26] N. Kasagi, Y. Tomita, and A. Kuroda. Direct numerical simulation of passive scalar field in a turbulent channel flow. *Journal of Heat Transfer*, 114(3):598–606, 08 1992. ISSN 0022-1481. doi: 10.1115/1.2911323. URL https://doi.org/10.1115/1.2911323.

[27] J. Kim, P. Moin, and R. Moser. Turbulence statistics in fully developed channel flow at low Reynolds number. *J. Fluid Mech.*, 177:133, 1987.

[28] K. Lam and S. Banerjee. On the condition of streak formation in a bounded turbulent flow. *Phys. Fluids*, 4(2):306–320, 1992.

[29] A.G. Lamorgese and R. Mauri. Diffuse-interface modeling of phase segregation in liquid mixtures. *Int. J. Multiph. Flow*, 34(10):987–995, 2008.

[30] L. Gary Leal. *Laminar Flow and Convective Transport Processes*. Butterworth-Heinemann, Boston, 1992. ISBN 978-0-7506-9117-8. doi: https://doi.org/10.1016/B978-0-7506-9117-8.50003-2.

[31] Zhaorui Li and Farhad A. Jaberi. Turbulence-interface interactions in a two-fluid homogeneous flow. *Physics of Fluids*, 21(9):095102, 2009. doi: 10.1063/1.3207860.

[32] S. L. Lyons, T. J. Hanratty, and J. B. McLaughlin. Large-scale computer simulation of fully developed turbulent channel flow with heat transfer. *Int. J. Numer. Methods Fluids*, 13(8):999–1028, 1991.

[33] F. Magaletti, F. Picano, M. Chinappi, L. Marino, and C.M. Casciola. The sharp-interface limit of the Cahn–Hilliard/Navier–Stokes model for binary fluids. *J. Fluid Mech.*, 714:95–126, 2013.

[34] N. N. Mansour, J. Kim, and P. Moin. Reynolds-stress and dissipation-rate budgets in a turbulent channel flow. *J. Fluid Mech.*, 194:15–44, 1988.

[35] Pierre Ricco, Claudio Ottonelli, Yosuke Hasegawa, and Maurizio Quadrio. Changes in turbulent dissipation in a channel flow with oscillating walls. *Journal of Fluid Mechanics*, 700:77–104, 2012. doi: 10.1017/jfm.2012.97.

[36] A. Roccon, M. De Paoli, F. Zonta, and A. Soldati. Viscosity-modulated breakup and coalescence of large drops in bounded turbulence. *Phys. Rev. Fluids*, 2:083603, 2017.

[37] A. Roccon, F. Zonta, and A. Soldati. Turbulent drag reduction by compliant lubricating layer. *J. Fluid Mech.*, 863:R1, 2019.

[38] Marco E. Rosti, Zhouyang Ge, Suhas S. Jain, Michael S. Dodd, and Luca Brandt. Droplets in homogeneous shear turbulence. *Journal of Fluid Mechanics*, 876: 962–984, 2019. doi: 10.1017/jfm.2019.581.

[39] W. Schoppa and F. Hussain. Coherent structure generation in near-wall turbulence. *J. Fluid Mech.*, 453:57–108, 2002.

[40] A. Soldati and S. Banerjee. Turbulence modification by large-scale organized electrohydrodynamic flows. *Phys. Fluids*, 10(7):1742–1756, 1998.

[41] G. Soligo, A. Roccon, and A. Soldati. Coalescence of surfactant-laden drops by Phase Field Method. *J. Comput. Phys.*, 376:1292–1311, 2019.

[42] G. Soligo, A. Roccon, and A. Soldati. Breakage, coalescence and size distribution of surfactant-laden droplets in turbulent flow. *J. Fluid Mech.*, 881:244–282, 2019.

[43] P. Than, L. Preziosi, D.D. Joseph, and M. Arney. Measurement of interfacial tension between immiscible liquids with the spinning road tensiometer. *J. Colloid Interface Sci.*, 124(2):552 – 559, 1988.

[44] C. M White and M.G. Mungal. Mechanics and prediction of turbulent drag reduction with polymer additives. *Annu. Rev. Fluid Mech.*, 40:235–256, 2008.

[45] P. Yue, J. Feng, C. Liu, and J. Shen. A diffuse-interface method for simulating two-phase flows of complex fluids. *J. Fluid Mech.*, 515:293–317, 2004.

A

Appendix

A.1 Interface Elevation

To further characterize the shape of the interface between the liquid layers, the probability density function (PDF) of the interface elevation, ζ/h has been determined, i.e. describing the difference between the local interface position and the nominal interface position ($z/h = 0.85$). The results are illustrated in Figure A.1. It is immediately apparent that crests and troughs of the interface are confined between $\zeta/h = -0.05$ and $\zeta/h = 0.05$. This indicates large fluctuations in interface position are unlikely to occur. This shows that the turbulent lubricating boundary layer is not able to deform the interface to a high degree in the presence of the laminar core flow. These findings are in agreement with the energy box results in Section 3.6 as the interfacial term contribution ($\overline{\psi_m}$), whose magnitude depends on the combined effect of the interface deformation and mean velocity, is small exceeding only 0.3% of the total energy input into the channel.

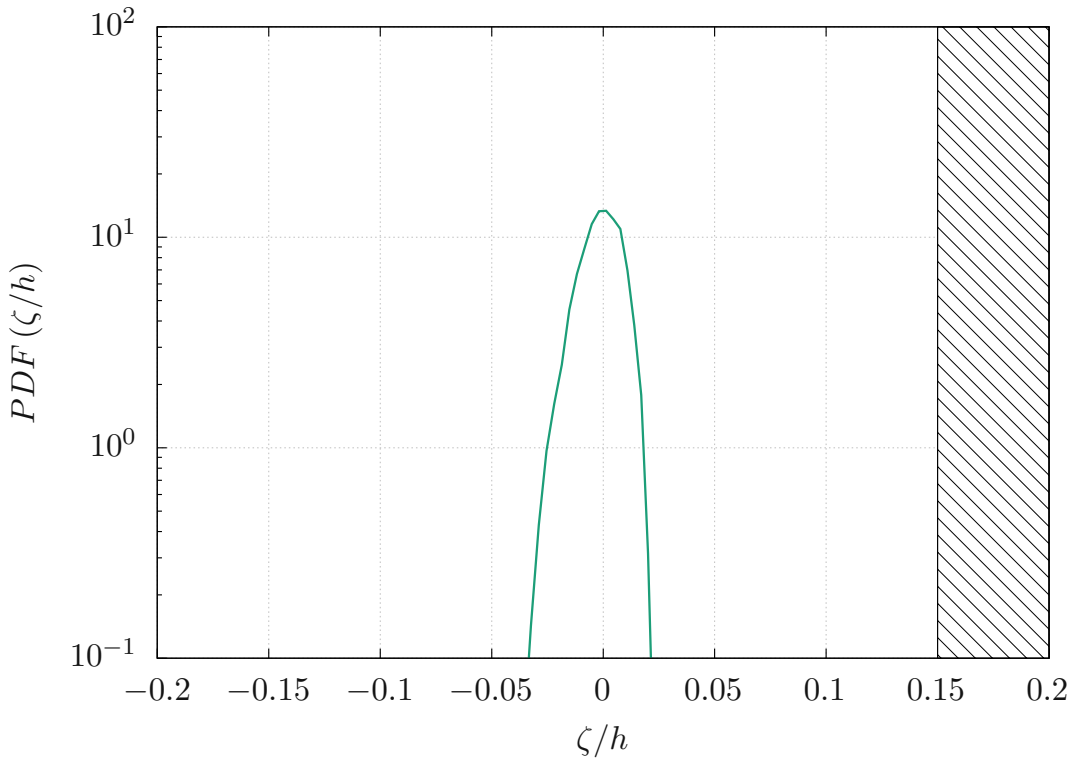

Figure A.1 – Probability density function (PDF) of the interface elevation ζ/h. Positive values of the interface elevation identify crests near the channel wall while negative values identify troughs oriented away from the channel wall. The hatched box identifies the channel wall boundary, i.e. $\zeta/h = 0.15$. Due to the symmetry of the problem only the symmetrized data of the interface elevation PDF is shown (——), to account for both liquid-liquid interfaces.

A.2 Additional Figures

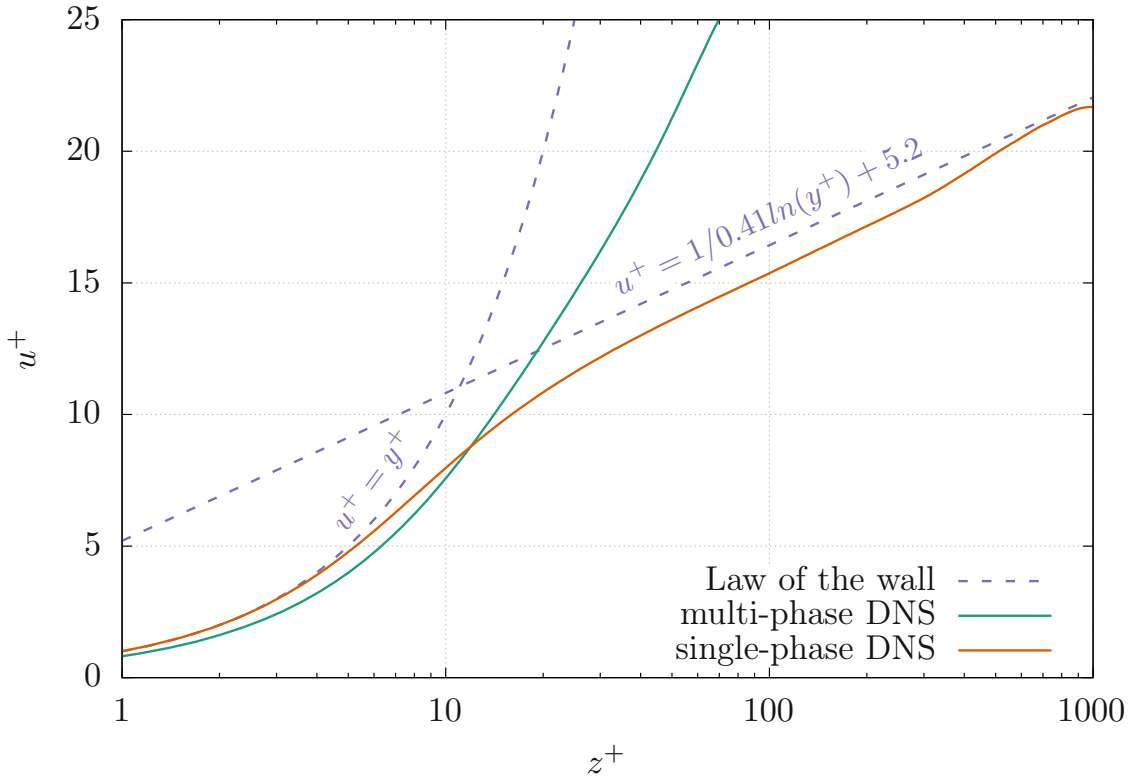

Figure A.2 – Comparison of simulation results with analytical boundary layer velocity profile.

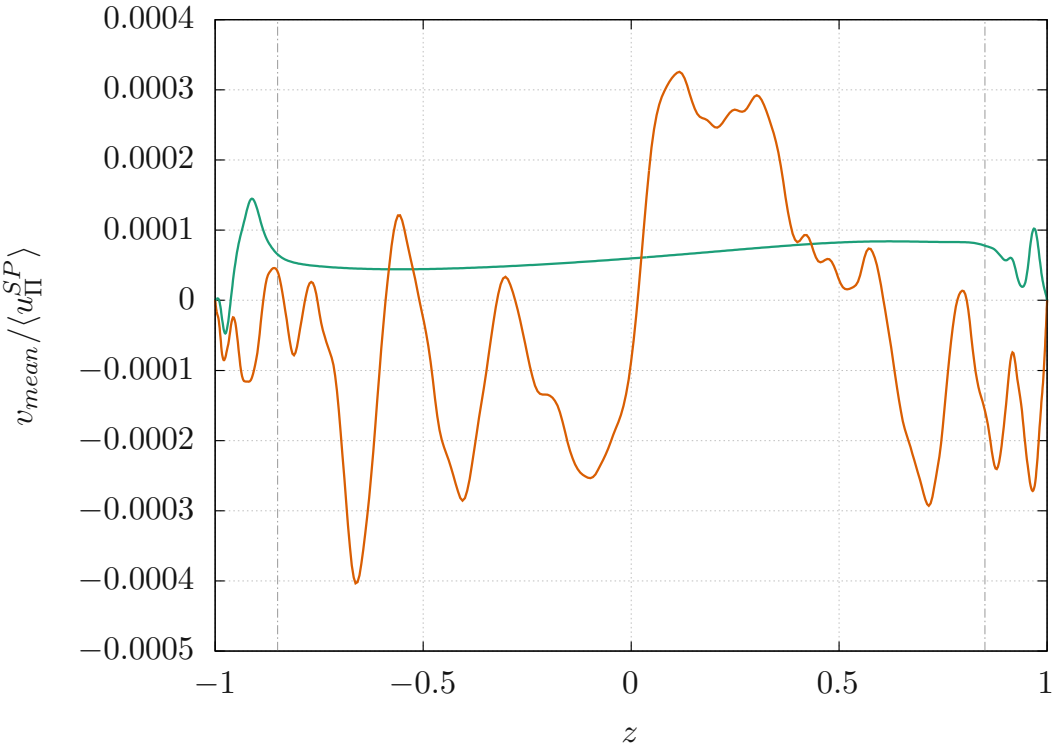

Figure A.3 – Comparison of the mean spanwise velocity v component over the channel height z between the lubricated channel (——) and the single-phase reference case (——). The velocity components are averaged in spanwise and streamwise directions. Furthermore the data is scaled to the power velocity of the single-phase reference flow $\langle u_\Pi^{SP}\rangle$. The nominal interface positions are marked with a gray dash-dotted line ($h = \pm 0.85$).

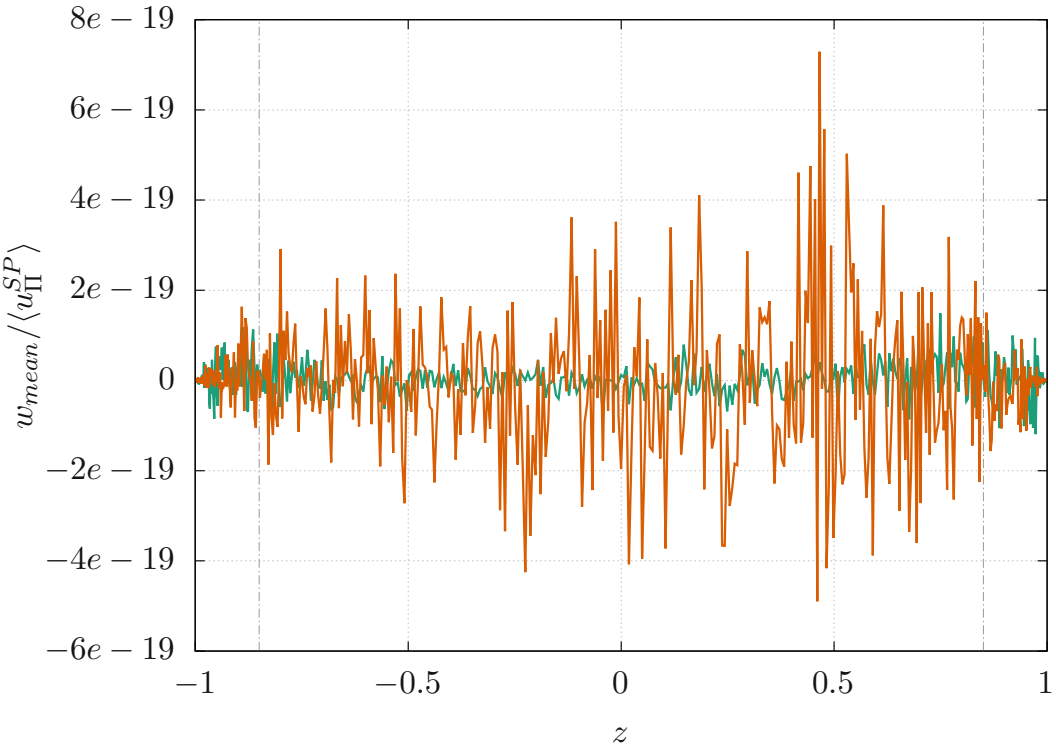

Figure A.4 – Comparison of the mean wall-normal velocity w component over the channel height z between the lubricated channel (—) and the single-phase reference case (—). The velocity components are averaged in span-wise and streamwise directions. Furthermore the data is scaled to the power velocity of the single-phase reference flow $\langle u_\Pi^{SP} \rangle$. The nominal interface positions are marked with a gray dash-dotted line ($h = \pm 0.85$).

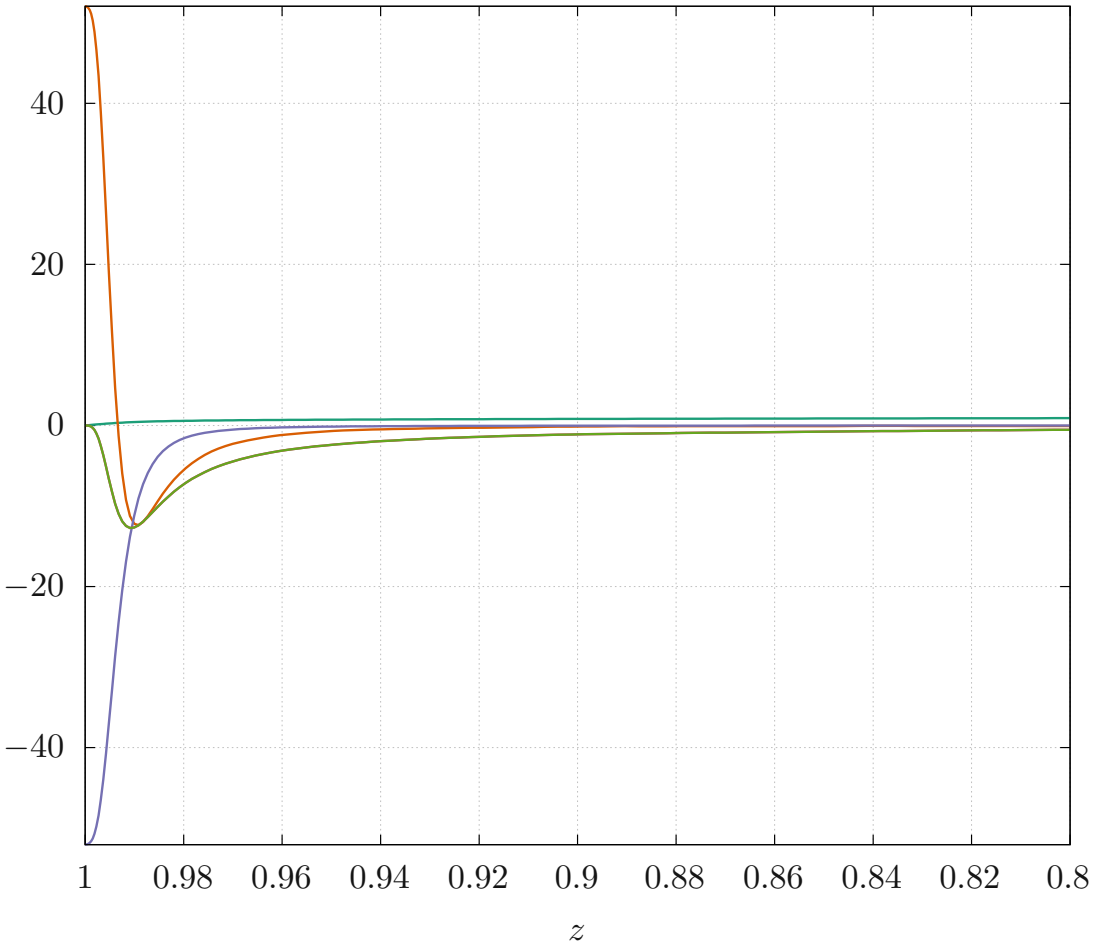

Figure A.5 – Mean kinetic energy component distribution for the single-phase reference channel. The different components are denoted by different colored lines: Pressure work Π_m (—), viscous diffusion D_m (—), mean viscous dissipation ϵ_m (—), TKE production P_k (—) and work performed by the Reynolds stresses T_m (—). The data is normalized to the total power injected into the system $\overline{\Pi_m}$.

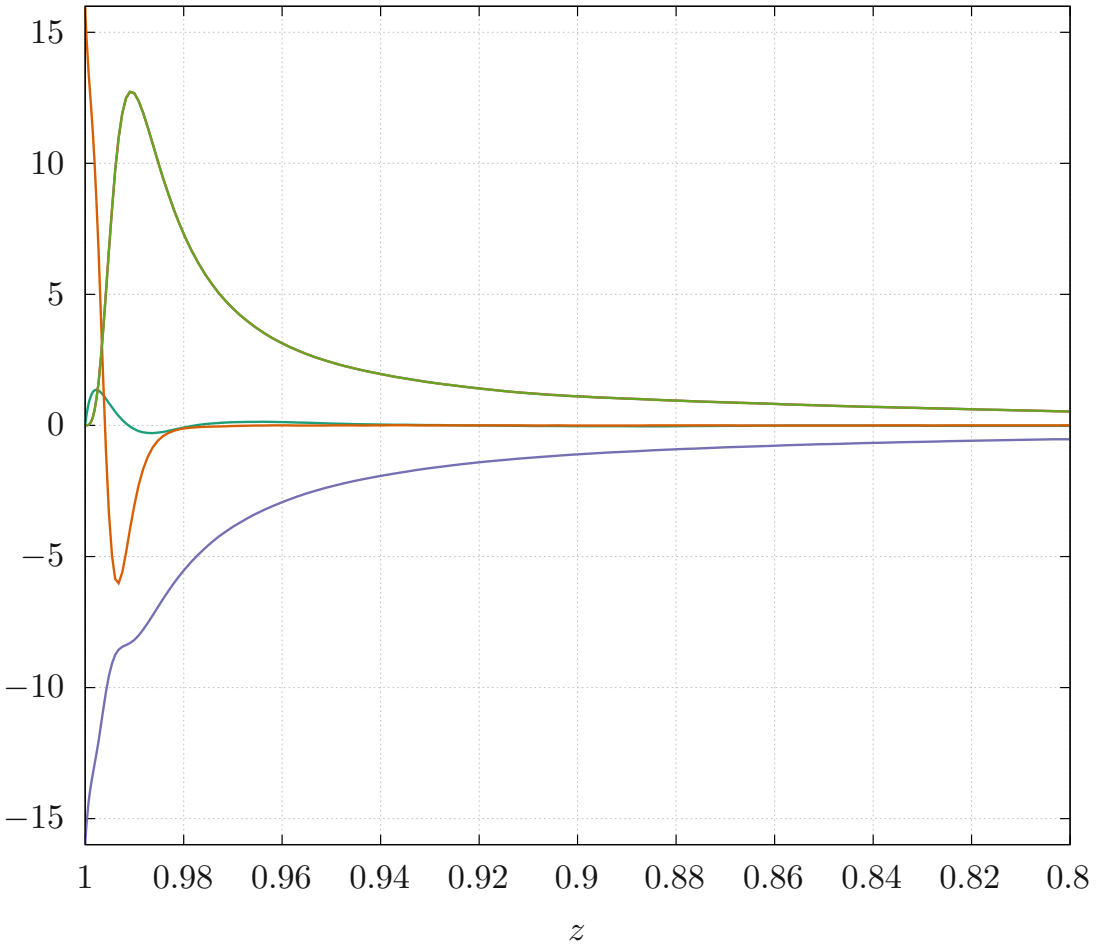

Figure A.6 – Turbulent kinetic energy component distribution for the single-phase reference channel. The different components are denoted by different colored lines: Pressure diffusion Π_k (—), viscous diffusion D_k (—), turbulent viscous dissipation ϵ_k (—), TKE production P_k (—) and turbulent diffusion T_k (—). The data is normalized to the total power injected into the system $\overline{\Pi_m}$.

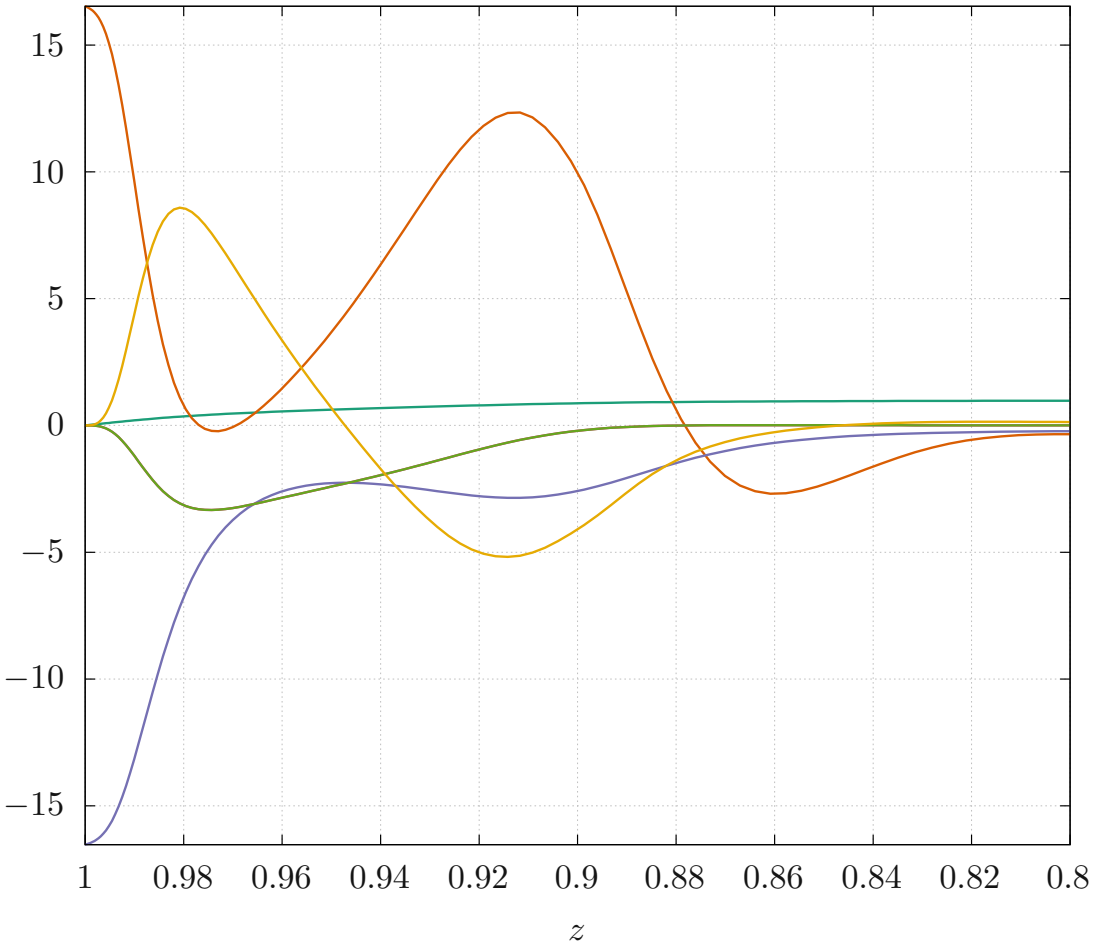

Figure A.7 – Mean kinetic energy component distribution for the lubricated channel: $\lambda = 0.01$. The different components are denoted by different colored lines: Pressure work Π_m (—), viscous diffusion D_k (—), mean viscous dissipation ϵ_m (—), TKE production P_k (—), work of the Reynolds stresses T_m (—) and the contribution of the interface term ϕ_m (—). The data is normalized to the total power injected into the system $\overline{\Pi_m}$.

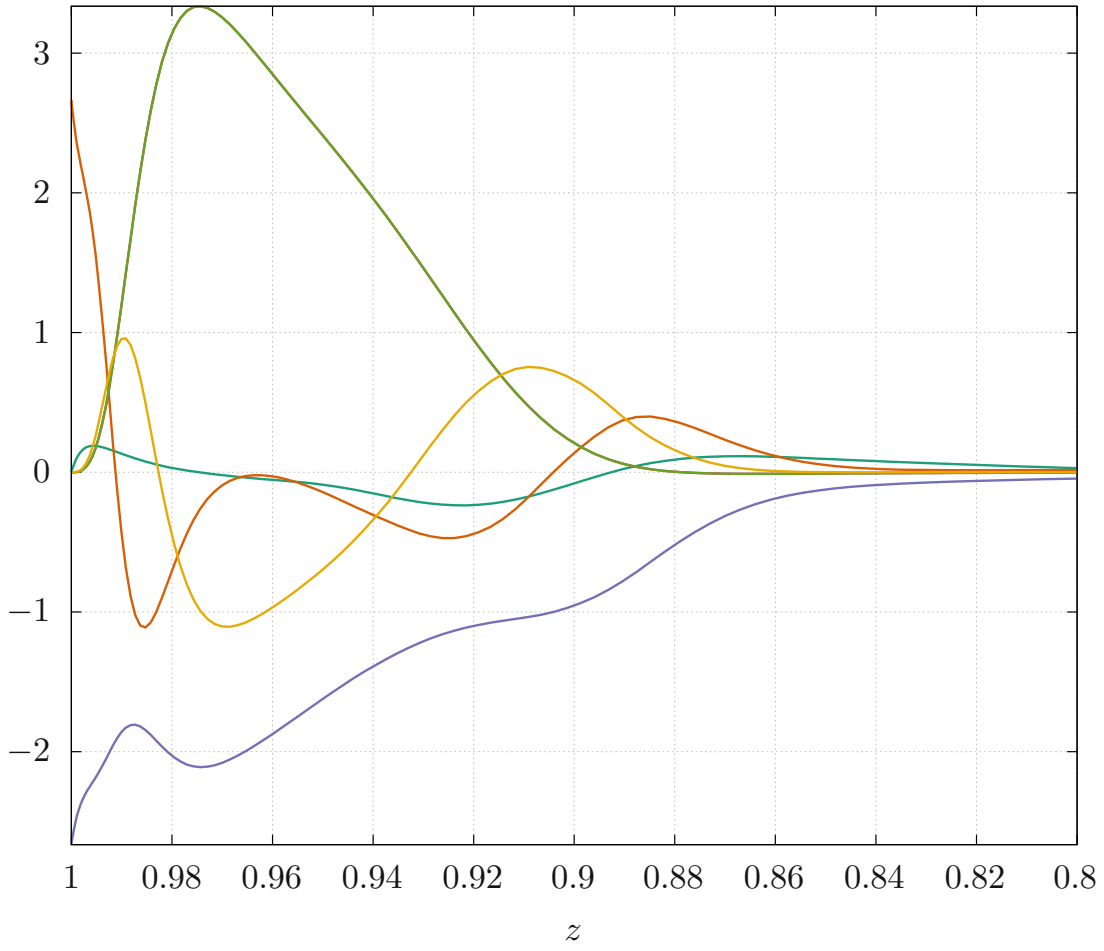

Figure A.8 – Turbulent kinetic energy component distribution for the lubricated channel: $\lambda = 0.01$. The different components are denoted by different colored lines: Pressure diffusion Π_k (—), viscous diffusion D_k (—), turbulent viscous dissipation ϵ_k (—), TKE production P_k (—), turbulent diffusion T_k (—) and the contribution of the interface term ϕ_k (—). The data is normalized to the total power injected into the system $\overline{\Pi_m}$.

Figure A.9 – Representation of the instantaneous interface position.